

Notice:

This manuscript has now been peer reviewed and published in *Geochemistry, Geophysics, Geosystems* following peer review, doi: <https://doi.org/10.1029/2020GC009092>.

Citation: Penney, C., Copley, A. (2021). Lateral variations in lower crustal strength control the temporal evolution of mountain ranges: Examples from south-east Tibet. *Geochemistry, Geophysics, Geosystems*, 22, e2020GC009092. <https://doi.org/10.1029/2020GC009092>

Details:

Title: Lateral variations in lower crustal strength control the temporal evolution of mountain ranges: examples from south-east Tibet

Authors:

Camilla Penney (COMET, University of Cambridge)

Alex Copley (COMET, University of Cambridge)

Contact: cp451@cam.ac.uk

1 Lateral variations in lower crustal strength control the
2 temporal evolution of mountain ranges: examples from
3 south-east Tibet

4 Camilla Penney^{1*}, Alex Copley¹

5 February 24, 2021

6 Key points:

- 7 • Lateral variations in lower crustal strength provide a first-order control on the shape
8 and temporal evolution of mountain ranges.
- 9 • Strong lower crust in the Sichuan Basin can explain the development of topography in
10 the Longmen Shan without a lower crustal channel.
- 11 • Lateral transport of samples should be considered in interpreting palaeoelevations from
12 stable-isotope palaeoaltimetry.

*Corresponding author: cp451@cam.ac.uk, ¹COMET, Bullard Laboratories, Department of Earth Sciences, University of Cambridge, Cambridge, UK

13 **Abstract**

14 Controversy surrounds the rheology of the continental lithosphere, and how this rheology
15 controls the evolution and behaviour of mountain ranges. In this study, we investigate
16 the effect of lateral contrasts in the strength of the lower crust, such as those between
17 cratonic continental interiors and weaker rocks in the adjacent deforming regions, on the
18 evolution of topography. We combine numerical modelling with recently published results
19 from stable-isotope palaeoaltimetry in south-east Tibet. Stable-isotope palaeoaltimetry in
20 this region provides constraints on vertical motions, which are required to distinguish between
21 competing models for lithosphere rheology and deformation. We use numerical modelling
22 to investigate the effect of lateral strength contrasts on the shape and temporal evolution
23 of mountain ranges. In combination with palaeoaltimetry results, our modelling suggests
24 that lateral strength contrasts provide a first-order control on the evolution of topography in
25 south-east Tibet. We find that the evolution of topography in the presence of such strength
26 contrasts leads to laterally-varying topographic gradients, and to key features of the GPS-
27 and earthquake-derived strain-rate field, without the need for a low-viscosity, lower-crustal
28 channel. We also find that palaeoaltimetric samples may have been transported laterally
29 for hundreds of kilometres, an effect which should be accounted for in their interpretation.
30 Our results are likely to be applicable to the evolution of mountain ranges in general, and
31 provide an explanation for the spatial correlation between cratonic lowland regions and steep
32 mountain range-fronts.

33 **Plain Language Summary**

34 The rocks which make up the Earth's continents move and change shape in response to
35 tectonic forces. How rocks respond to these forces depends on their material properties,
36 which can vary in space and time. These material properties, therefore, control the shape

37 of mountain ranges, and how mountains grow. This study investigates why some mountain
38 ranges have steep fronts, whilst others have gentle gradients. We look at how regions made
39 up of strong rocks (such as the Sichuan Basin) affect the shape and growth of adjacent
40 mountain ranges. We find that mountain ranges with steep fronts can form when weaker
41 rocks move over stronger ones. Recent measurements of oxygen in ancient soils suggests that
42 parts of the south-eastern margin of the Tibetan Plateau (between the Sichuan Basin and
43 the Central Lowlands of Myanmar) have been high since about 50 million years ago, and
44 that the area has risen more slowly than has previously been estimated. In south-east Tibet,
45 the pattern of earthquakes, and how fast the mountains have grown, can be explained by
46 these strong areas, without invoking complicated material properties in the mountain ranges.
47 Such strong regions may be important in controlling the shape of mountain ranges globally.

48 **1 Introduction**

49 The strength of the lithosphere provides a first-order control on the distribution of strain
50 within it. Strength, here, means resistance to deformation, which might be controlled by
51 the stresses transmitted across faults in the brittle part of the lithosphere or the rheology
52 associated with ductile creep in the mid-to-lower crust and upper mantle. Lateral strength
53 contrasts, such as those between cratonic continental interiors made of cool, anhydrous
54 rocks (from which volatiles have been removed by previous partial melting) and the adja-
55 cent deforming regions made of hotter and more hydrous rocks, are a feature of continental
56 lithosphere globally. Such contrasts control the distribution of strain in the continents and,
57 therefore, the evolution of mountain ranges (e.g. Vilotte et al., 1984; England and Houseman,
58 1985; Flesch et al., 2001; Jackson et al., 2008). Regions with strong crust, such as cratons,
59 tend to accommodate little strain in comparison to their surroundings. In the India–Eurasia
60 collision, for example, it is the accreted terranes which form the southern margin of Eura-

61 sia, rather than cratonic India, which have accommodated most of the shortening. Here we
62 investigate the effect of lateral contrasts in the strength of the lower crust on the temporal
63 evolution of mountain belts.

64

65 A key outstanding question about the effect of lateral strength contrasts is how regions
66 with strong lower crust, and the flow of less viscous material over and around them, affect
67 the evolution of mountain ranges over tens of millions of years. Previous studies of con-
68 tinental deformation demonstrate that models which are able to reproduce instantaneous
69 strain rates do not necessarily lead to the formation of the observed topography over time
70 (e.g. Houseman and England, 1986; England and Houseman, 1986), so incorporating tempo-
71 ral evolution is an important extension to models considering the geologically-instantaneous
72 effects of strength contrasts (e.g. Copley, 2008; Bischoff and Flesch, 2019). This paper
73 concerns the physical controls on mountain building, and the constraints which recently-
74 published stable-isotope palaeoaltimetry observations can provide on lithosphere rheology.
75 Vertical motions, to which palaeoaltimetry observations are sensitive, have the potential to
76 distinguish between rheological models which lead to the same horizontal surface velocities
77 (Copley, 2008; Flesch et al., 2018). Understanding the implications of these observations,
78 and the associated caveats is, therefore, critical to constraining lithosphere rheology. Nu-
79 merical models with a small number of parameters allow us to test whether lower-crustal
80 strength contrasts, consistent with geological and geodetic observations, can reproduce lat-
81 eral variations in topographic gradients, or whether other driving mechanisms are required.
82 In this study, we combine recently-published palaeoaltimetry observations from south-east
83 Tibet with a simple 3D model of crustal deformation, to explore the effects of lateral strength
84 contrasts on continental deformation.

85

86 The south-eastern margin of the Tibetan plateau (here referred to as ‘south-east Tibet’),

87 Figure 1) is a good place to study the effect of lateral strength contrasts. Low elevations,
88 relief and strain rates (both seismic – Figure 1 – and geodetic – Zheng et al., 2017; Mau-
89 rin et al., 2010) in the Sichuan Basin and the Central Lowlands of Myanmar suggest that
90 these regions experience relatively little deformation. These regions are, therefore, likely to
91 be strong in comparison to the high region between them, and the mountain belts which
92 surround them, which have undergone significant recent and cumulative deformation. The
93 Sichuan Basin is covered by ~ 10 km of sediments (Hubbard and Shaw, 2009), underlain
94 by Paleoproterozoic crust (Burchfiel et al., 1995) with high seismic velocities in the upper
95 mantle (e.g. Lebedev and Nolet, 2003; Li and Van Der Hilst, 2010). Post-seismic motion
96 after the 2008 Wenchuan earthquake suggests a strength contrast across the Longmen Shan
97 (Huang et al., 2014), as do differences in elastic thickness between the Longmen Shan and
98 the Sichuan Basin, estimated from gravity anomalies (Fielding and McKenzie, 2012).

99

100 Although the Central Lowlands of Myanmar have been less extensively studied than the
101 Longmen Shan, the lack of topography, and the presence of undeformed Miocene sediments
102 suggest low rates of post-Miocene deformation (Wang et al., 2014). Initial GPS measure-
103 ments by Maurin et al. (2010) suggest that central Myanmar, west of the Sagaing fault,
104 deforms in a coherent manner. Earthquakes in the Central Lowlands of Myanmar, shown in
105 Figure 1b, are associated either with strike-slip motion on the Sagaing fault, on the eastern
106 margin of the lowlands (which accommodates a component of the oblique India–Eurasia con-
107 vergence; Maurin et al., 2010), or with active subduction beneath the Indo-Burman ranges
108 (e.g. Stork et al., 2008; Steckler et al., 2016, yellow focal mechanisms in Figure 1b have
109 depths > 50 km). The seismic strain rate within the Central Lowlands is, therefore, low, at
110 least in the instrumental period.

111

112 In contrast, the high regions of south-east Tibet deform rapidly, with kinematics de-

113 scribed in detail by Copley (2008), who also summarised the work of previous authors. Since
114 that study, numerous thrust-faulting earthquakes have occurred along the Longmen Shan,
115 including the 2008 Wenchuan and 2013 Lushan earthquakes and their aftershocks (Figure 1).
116 These earthquakes, and subsequent analysis of shortening on structures imaged in seismic
117 profiles (Hubbard and Shaw, 2009), demonstrate that active shortening of the brittle upper
118 crust is occurring across the Longmen Shan.

119

120 Much of the morphology of south-east Tibet is dominated by deeply-incised river valleys,
121 often following strike-slip faults (Wang and Burchfiel, 1997). Collectively these strike-slip
122 faults accommodate south-eastwards motion of high topography relative to both the Sichuan
123 Basin and the Central Lowlands of Myanmar (e.g. Shen et al., 2005), with the faults on op-
124 posite sides of the high region accommodating opposite senses of shear (Figure 1a). The
125 Xianshuihe and Sagaing faults (Figure 1a) have left- and right-lateral geodetic slip rates of
126 $\sim 7\text{--}9\text{ mm yr}^{-1}$ and $\sim 18\text{ mm yr}^{-1}$ respectively (Zheng et al., 2017; Maurin et al., 2010).
127 The region of distributed left-lateral faulting east of the Sagaing fault (Figure 1a) accom-
128 modates right-lateral shear on north-south striking planes through rotations about vertical
129 axes (Copley, 2008).

130

131 A suite of models (e.g. Royden et al., 1997; Clark and Royden, 2000; Clark et al., 2005a;
132 Burchfiel et al., 2008) have focussed on the possibility of flow in a low viscosity, lower-crustal
133 channel as an explanation for the steep topography of the Longmen Shan and the gentle
134 topographic gradients to the south of the basin. By extending these channel-flow models to
135 include rigid regions, Cook and Royden (2008) argued for the importance of both a strong
136 Sichuan Basin, and flow in a mid-lower crustal channel in the formation of steep topography
137 across the Longmen Shan. Chen et al. (2013a) and Chen et al. (2013b) used 2D thermo-
138 mechanical models with extrapolated laboratory flow laws to demonstrate that the craton

139 was an important control on deformation in the region. We build up on this work by using
140 a simple 3D model to isolate the effects of this rigid, cratonic region, and by comparing the
141 results to observational constraints from palaeoaltimetry.

142

143 Vertical velocities can distinguish between competing models of depth-dependent rheol-
144 ogy which would lead to the same horizontal velocities (Copley, 2008; Flesch et al., 2018;
145 Bischoff and Flesch, 2019). Copley (2008) demonstrated that rapid flow at depth associated
146 with a weak mid-to-lower crust in the Longmen Shan would lead to faster instantaneous
147 vertical motions than coherent upper- and lower- crustal deformation. The specific rates
148 were based on instantaneous calculations, so would not necessarily apply to the geologically-
149 recorded uplift rates, but exemplify the possibility of using vertical motions to distinguish
150 between different models of depth-dependent rheology.

151

152 Many quantitative studies of topographic evolution in south-east Tibet have focussed
153 on thermochronology (e.g. Kirby et al., 2002; Clark et al., 2004; Wang et al., 2012, 2016).
154 Thermochronometric ages give information about exhumation, which is controlled by the in-
155 terplay between tectonics and erosion. Such ages have been interpreted to imply that rapid
156 uplift occurred $\sim 13\text{--}5$ Ma, based on the identification of geomorphic surfaces presumed to
157 have formed at low elevation (Clark et al., 2005a, 2006). However, it has been suggested
158 that such low-relief, erosional surfaces can also form at high elevations (e.g. Liu-Zeng et al.,
159 2008; Yang et al., 2015) and that increased exhumation may have been related to changes
160 in the base level of rivers draining the region rather than tectonic uplift (e.g. Richardson
161 et al., 2008). The interpretation of the existing thermochronometric data in terms of eleva-
162 tion history is therefore unclear. In this study we make use of recently-published estimates
163 of palaeoelevation from stable-isotope geochemistry, which provide an opportunity to quan-
164 titatively constrain the elevation history of south-east Tibet and, therefore, to distinguish

165 between competing models of lithosphere rheology and mountain-range evolution.

166

167 We first summarise recently-published results from stable-isotope palaeoaltimetry (Sec-
168 tion 2) to constrain the uplift and elevation history of south-east Tibet. We then use fluid-
169 dynamical modelling of the mountain range (described in Section 3) to investigate the effects
170 of lateral strength contrasts on the evolution of topography through time, and compare our
171 results to south-east Tibet (Section 4).

172

173 Although the results presented here are in the context of south-east Tibet, the presence
174 of lateral strength contrasts is a common feature of mountain ranges globally (e.g. Lamb,
175 2000; Jackson et al., 2008; Dayem et al., 2009b,a; Nissen et al., 2011). In particular, many
176 mountain ranges, both active and older, have edges adjacent to cratons (e.g. McKenzie and
177 Priestley, 2008); regions of (often thick) continental lithosphere, usually composed of Pro-
178 toerozoic or Archean crust, which have remained relatively undeformed by tectonic events on
179 their margins (Holmes, 1965). In section 5, therefore, we discuss the applicability of our
180 results to the temporal evolution of mountain ranges in general.

181

182 **2 Palaeoaltimetry**

183 Stable-isotope palaeoaltimetry uses systematic variations in the isotopic composition of pre-
184 cipitation (usually $\delta^{18}O$) with elevation to derive the palaeoelevation of sample sites (e.g.
185 Rowley et al., 2001). These techniques have been developed in order to place quantitative
186 constraints on the elevation history of orogenies, such as Tibet, but they have not yet been
187 extensively used as a constraint in dynamic models.

188

189 South-east Tibet is a good region to carry out palaeoaltimetry studies. Moisture paths
190 from the ocean to high topography in this region are simple, as shown by the Rayleigh frac-
191 tionation relationship between the oxygen-isotope composition of precipitation and elevation
192 in present-day elevation transects (Hren et al., 2009).

193

194 Figure 2 shows results from seven recent palaeoaltimetry studies in south-east Tibet,
195 which use soil-deposited (Hoke et al., 2014; Xu et al., 2016; Tang et al., 2017; Gourbet
196 et al., 2017; Xiong et al., 2020) and/or lacustrine (Li et al., 2015; Xu et al., 2016; Gourbet
197 et al., 2017; Wu et al., 2018) carbonates to derive the oxygen-isotope composition of palaeo-
198 precipitation and, hence, palaeoelevations. In south-east Tibet, the age of sampled forma-
199 tions is a significant source of uncertainty (Hoke, 2018). Gourbet et al. (2017) and Li et al.
200 (2020) have recently revised the ages of formations in the Jianchuan and Lühe basins respec-
201 tively (Figure 2b). In the most extreme cases, the revised dating has shown that formations
202 previously mapped as mid-to-late Miocene were deposited in the late Eocene (Gourbet et al.,
203 2017). Hotter global temperatures in the Eocene (Savin, 1977; Miller et al., 1987; Zachos
204 et al., 2001) alter the relationship between isotopic composition and elevation, resulting in
205 multiple paleoelevation estimates for some samples, depending on which relationships were
206 used (filled and unfilled symbols in Figure 2b show paleoelevation estimates calculated using
207 modern and Eocene relationships respectively). However, the differences in palaeoelevation
208 resulting from whether hotter temperatures are used are generally much less than the kilo-
209 metre scale of interest for dynamic modelling, even for upper-bound estimates of Eocene
210 temperature (region 4, Figure 2b, Hoke et al., 2014; Li et al., 2015; Tang et al., 2017; Wu
211 et al., 2018).

212

213 The oxygen-isotope ratio at sea level is also time-dependent. Licht et al. (2014) found
214 very negative values of $\delta^{18}O$ in an Eocene gastropod and rhinocerotid from Myanmar, taken as

215 sea level references for the time. Preliminary results from isotopic analysis of soil-deposited
216 carbonates in the same area show similarly low $\delta^{18}O$ (Licht et al., 2019). A more negative
217 starting value leads to lower palaeoelevation estimates, since Rayleigh fractionation predicts
218 increasingly negative $\delta^{18}O$ with elevation. These improved estimates of sea-level composi-
219 tion, as well as the dating discussed above, have led to recalculations of palaeoelevation in
220 south-east Tibet (Gourbet et al., 2017; Wu et al., 2018, shown as black symbols in Figure 2b-
221 4, the original estimates are shown in gray), and we use these in our uplift rate calculations.

222

223 Uplift rates can be derived from stable-isotope palaeoaltimetry if samples can be taken
224 from rocks of multiple ages at the same location or compared with the present-day elevation
225 (blue dashed lines in Figure 2b). These rates, therefore, only reflect points in space and
226 time which are preserved in the carbonate record. Where such rates can be inferred they are
227 shown in Figure 2b. All but one of these inferred uplift rates are $<0.3\text{mm yr}^{-1}$.

228

229 In most of the regions shown in Figure 2, paleoelevations similar to present-day eleva-
230 tions are found in the oldest sampled formations. To the north-west (region 1), Tang et al.
231 (2017) suggest that topography may have been high since before the Eocene. Xiong et al.
232 (2020) also found high topography in the Gonjo basin by the late Eocene, though their
233 results suggest that this uplift may have occurred during the Eocene, giving possible early
234 Eocene uplift rates of up to 0.8 mm yr^{-1} , the only uplift rate $>0.3\text{ mm yr}^{-1}$ in the studies
235 reviewed here. Although Xu et al. (2016)'s measurements have significant uncertainty in
236 the moisture source, they suggest a lower bound for the elevation of the Longmen Shan
237 in the late Miocene of $\sim 3000\text{ m}$, compared to present-day elevations of $2800\text{-}3700\text{ m}$. To
238 the south-east, region 5 may have experienced some uplift since the late Miocene, at rates
239 $<0.3\text{ mm yr}^{-1}$, and region 6 is likely to have been at its present elevation by the late Miocene.

240

241 These stable-isotope palaeoaltimetry results suggest that at least some areas of present-
242 day south-east Tibet have been high since the late Eocene, and are likely to have reached
243 present-day elevations prior to the onset of rapid exhumation inferred by Clark et al. (2005b)
244 from the incision of river gorges (gray region in Figure 2b). Uplift rates across south-east
245 Tibet are likely to have been much lower ($<0.3 \text{ mm yr}^{-1}$) than would be predicted if all the
246 topographic growth in the region had occurred since the late Miocene. Recently published
247 thermochronology is also consistent with this palaeoaltimetric data, suggesting that topog-
248 raphy across the Longmen Shan had begun to develop by the Oligocene (Wang et al., 2012),
249 and that uplift may have been ongoing since the Paleocene (Liu-Zeng et al., 2018).

250

251 **3 Dynamical modelling**

252 In tandem with the palaeoaltimetry estimates summarised in section 2, we use numeri-
253 cal modelling to investigate the effect of lateral contrasts in lower crustal strength on the
254 temporal evolution of mountain ranges. We first summarise the work of previous authors
255 (section 3.1) and then describe the setup for the model used here (section 3.2) and our
256 boundary conditions (section 3.3), before describing the model results in section 4. Our
257 model is designed to investigate the first-order effects of lateral strength contrasts on the
258 multi-million-year development of long-wavelength topography in general, rather than to
259 simulate the detailed evolution of south-east Tibet.

260

261 **3.1 Previous Models**

262 In regions of distributed deformation, the continental lithosphere can be modelled as a con-
263 tinuum (commonly a viscous fluid), with motion driven by horizontal pressure gradients

264 – resulting from gravity acting on elevation contrasts – and by the relative motion of the
265 bounding plates (e.g. England and McKenzie, 1982, 1983; Houseman and England, 1986;
266 Royden et al., 1997; Lamb, 2000; Flesch et al., 2001; Reynolds et al., 2015; Flesch et al.,
267 2018). Many authors use the thin-viscous-sheet model, which assumes negligible depth vari-
268 ations in horizontal velocities (England and McKenzie, 1982, 1983). This model implicitly
269 assumes that the top and base of the lithosphere experience shear tractions which are small
270 in comparison to normal components of the deviatoric stress tensor (here referred to as a
271 stress-free basal boundary condition, after McKenzie et al., 2000). In the thin-viscous-sheet
272 model, this corresponds to flow over a less viscous fluid (the asthenosphere). Such models can
273 only produce steep-fronted topography if the lithosphere has an effective power-law rheology
274 with a high stress exponent (typically greater than 3, i.e. shear-thinning, e.g. Houseman
275 and England, 1986; Lechmann et al., 2011). The typical topographic gradients produced
276 by these models are still much less steep than those in steep-fronted mountain ranges such
277 as the Himalayas and the Longmen Shan (England and Houseman, 1986). Geologically,
278 stress exponents greater than 1 are associated with rocks deforming by dislocation creep
279 (e.g. Stocker and Ashby, 1973, discussed further in Section 5).

280

281 Step topographic gradients often occur adjacent to lateral contrasts in lithosphere strength.
282 Such regions are commonly associated with large gradients in crustal thickness, and, if less
283 viscous material flows over a much higher viscosity region, this is equivalent to flow over a
284 rigid base (referred to here as a no-slip basal boundary condition, defined as zero-horizontal
285 velocity after McKenzie et al., 2000). In such regions the thin-viscous sheet approxima-
286 tion breaks down, because flow over a rigid base is accommodated by vertical gradients of
287 horizontal velocity in the flowing layer. Medvedev and Podladchikov (1999a) presented an
288 extension to the thin-viscous sheet model to allow for rapid spatial variations in material
289 properties, which was applied to 2D geodynamic scenarios by Medvedev and Podladchikov

290 (1999b). An alternative approach is to use full thermo-mechanical models in either 2D (e.g.
291 Beaumont et al., 2001) or 3D (e.g. Lechmann et al., 2011; Pusok and Kaus, 2015). Here we
292 discuss a simplified approach, which allows us to incorporate flow over both stress-free and
293 rigid boundaries into a single 3D model with a small number of adjustable parameters.

294

295 Previous studies incorporating vertical gradients of horizontal velocity have focused on
296 reproducing geologically-instantaneous deformation in south-east Tibet (e.g. Copley, 2008;
297 Lechmann et al., 2014; Bischoff and Flesch, 2019). These studies have demonstrated that key
298 features of the instantaneous earthquake- and GPS-derived velocity field can be explained
299 by lateral viscosity contrasts between cratonic blocks and the surrounding mountain ranges.
300 Studies which have investigated the effects of these cratonic blocks on the temporal evolution
301 of topography in south-east Tibet have used complex models at the scale of entire collision
302 zones (e.g. Pusok and Kaus, 2015), or imposed external forcing or velocities to drive the
303 flow (e.g. Cook and Royden, 2008). Here, we use a simple model of 3D crustal deformation,
304 described below, to isolate the effects of lateral strength contrasts on the evolution of topog-
305 raphy through time. Our interest is in understanding the physical controls on topographic
306 evolution, in particular the development of laterally contrasting topographic gradients. Con-
307 sideration of the temporal evolution of the topography is important because it allows us to
308 investigate the constraints which can be provided by the newly-available palaeoaltimetry
309 data.

310

311 **3.2 Model Setup**

312 We model the lithosphere as a viscous fluid. The geometry and boundary conditions we
313 use are based on the long-wavelength topography of south-east Tibet (Figure 3). Using a
314 geometry similar to south-east Tibet allows us to make use of the palaeoaltimetric results

315 described in Section 2 in assessing the uplift rates in the model.

316

317 GPS velocities (relative to Eurasia) in south-east Tibet are sub-parallel to topographic
318 gradients (Figure 3). Movement of material along topographic gradients suggests that the
319 deformation in south-east Tibet is governed by gravitational potential energy gradients. The
320 models we investigate here are, therefore, driven by gravity acting on crustal thickness con-
321 trasts, without applied compressive forces or imposed boundary velocities. This category of
322 models has been described by Lechmann et al. (2014) as “density driven”. Analogous models
323 have been applied since the 1980s to the gravitational spreading of crustal thrust sheets (e.g.
324 Ramberg, 1981; Merle and Guillier, 1989). Here we consider deformation on the lithosphere
325 scale, rather than the lengthscale of individual thrust sheets. These earlier studies also con-
326 sidered analogues between glaciological and geological gravity-driven deformation, including
327 the possibility of both stress-free and no-slip basal boundary conditions (Ramberg, 1981).
328 We extend this analogy here by using methods developed for ice-sheet modelling to solve the
329 governing equations.

330

331 We solve a simplified form of the Stokes’ equations using the method proposed by Pattyn
332 (2003), which includes vertical gradients of horizontal velocities. This method allows us to
333 model flow over a stress-free base and also a no-slip base, representing regions of strong lower
334 crust, unlike traditional thin-viscous-sheet models (England and McKenzie, 1982, 1983). The
335 implementation and more mathematical details of this approach are given in Appendix A.

336

337 The method we use here has previously been used to calculate instantaneous strain rates
338 in south-east Tibet (Copley, 2008). Reynolds et al. (2015) extended this approach to model
339 the temporal evolution of the Sulaiman Ranges by re-writing the incompressibility condi-
340 tion as a diffusion equation for topography (Pattyn, 2003). We use an improved method

341 (Appendix A) to solve this diffusion equation, calculating diffusivities on a staggered grid,
342 and using the generalised minimum residual method (Saad and Schultz, 1986) to solve the
343 resulting sparse matrix equations. We use a regular horizontal grid of 15 km×15 km, and
344 20 grid points in the vertical, which are re-scaled at each time step (Appendix A; Pattyn,
345 2003). The assumptions and set-up of this model are discussed below.

346

347 We model the deforming crust as an isoviscous, Newtonian fluid. Using a simple rheology
348 allows us to test the extent to which topographic evolution in south-east Tibet is controlled
349 by the presence of lateral lower crustal strength contrasts, and whether additional rheological
350 complexity is required to explain the geophysical and geological observations. The simple
351 rheology we use contrasts with the approach of previous authors studying the effect of a
352 strong craton on the evolution of topography in south-east Tibet. For example, Chen et al.
353 (2013a) used a 2D model with multiple rock types and an assumed geotherm. Cook and
354 Royden (2008) included a weak lower crustal channel and drove deformation within their
355 model through an imposed velocity at its base. By using a simpler rheology, we are able
356 to isolate the effects of lower crustal strength contrasts on the evolution of topography. We
357 discuss the possible effects of a more complicated rheology in Section 5. The equations re-
358 lating velocities in the fluid to gradients in topography are linearly dependent on the fluid
359 viscosity (Appendix A) so although we use a viscosity of 10^{22} Pas here (as suggested for
360 south-east Tibet by Copley and McKenzie, 2007), we expect that these models will apply to
361 different viscosities with scaled times and velocities. For example, we expect the topography
362 after 50 Myr of model evolution with a viscosity of 10^{22} Pas to be the same as that after
363 5 Myr for a viscosity of 10^{21} Pas. The velocities would be 10 times greater in the 10^{21} Pas case.

364

365 We impose Airy isostatic compensation at the base of the crust, relative to a column
366 of mantle (Flesch et al., 2001), with crust and mantle densities $\rho_c = 2700 \text{ kg m}^{-3}$ and

367 $\rho_m = 3300 \text{ kg m}^{-3}$ respectively, giving a ratio of crustal-root depth to topographic elevation
368 of 4.5 (f in Figure 4). Assuming Airy isostatic compensation neglects flexural support of
369 the topography. By using a viscous model, we are implicitly considering long-wavelength
370 deformation (motivated by the long-wavelength shape of the topography in Figure 3). Free-
371 air gravity anomalies from south-east Tibet (Fielding and McKenzie, 2012) suggest that
372 flexure plays a role in supporting the topography on relatively short wavelengths ($\sim 50 \text{ km}$
373 into the Longmen Shan), which means that isostatic compensation is an appropriate as-
374 sumption throughout most of the model domain. At the edge of the basin region, where
375 flexural support may be important, flexure would be expected to give a shape for the basal
376 boundary that is intermediate between full isostatic compensation, which we use here, and
377 a base which cannot move vertically in response to loading, a case which is often considered
378 in the fluid dynamics literature (e.g. Huppert, 1982). The implications of assuming isostatic
379 compensation are discussed in Section 4.

380

381 Figure 4 shows a diagram of our model setup. High viscosity regions, analogous to the
382 strong lower crust of the Sichuan Basin and the Central Lowlands of Myanmar, are simu-
383 lated by setting horizontal velocities to zero in part of the model with a specified thickness
384 (“basal thickness”, grey areas in Figure 4). Flow can occur over and around these rigid
385 regions (“basins”, Basin E and Basin W in Figure 4), which deform vertically according to
386 Airy isostatic compensation. The basal thickness is equivalent to the thickness of strong
387 lower crust. The Sichuan Basin is connected to the South China craton (e.g. Li and Van
388 Der Hilst, 2010), which provides a resistive force, so the basins in our model are not ad-
389 vected with the flow. By setting velocities to zero in these basin regions, we are assuming
390 that the lower crust in the Sichuan Basin and Central Lowlands of Myanmar has behaved
391 rigidly over the 50 Myr of deformation which we model. This approach is supported by
392 inferences of strong lower crust and upper mantle in the Sichuan Basin and Central Low-

393 lands of Myanmar (Section 1; Li and Van Der Hilst, 2010; Huang et al., 2014). An estimate
394 of the lower crustal viscosity required for our assumption of rigidity to hold true can be
395 calculated from the gravitational potential energy contrast between the Longmen Shan and
396 Sichuan Basin. The crustal thicknesses in the Longmen Shan and Sichuan Basin are 65
397 and 36–40 km respectively (e.g. Liu et al., 2014), with 4.5 km of elevation contrast. The
398 horizontal force associated with these variations of crustal thickness can be estimated from
399 variations of gravitational potential energy between the two columns of crust (both of which
400 are in Airy isostatic equilibrium with a column of mantle, e.g. Artyushkov, 1973; Molnar
401 and Tapponnier, 1978; Dalmayrac and Molnar, 1981; Molnar and Lyon-Caen, 1988), giving
402 a maximum horizontal force of 7×10^{12} N m⁻¹, similar to that applied by Tibet on cratonic
403 India (e.g. Molnar and Lyon-Caen, 1988; Copley et al., 2010). Assuming that this force is
404 distributed uniformly with depth in the crust, this horizontal force results in a maximum
405 deviatoric normal stress acting on the Sichuan Basin of ~ 120 MPa. This stress, and therefore
406 the required viscosity, would be lower if any of the stress were supported by the mantle. If
407 this topographic contrast has existed since 50 Mya (the effective start time of our model)
408 then for the Sichuan Basin, which is ~ 300 km wide, to have deformed by less than one grid
409 cell in our model (15 km), requires a strain rate in the lower crust less than 3.2×10^{-17} s⁻¹.
410 In this scenario the viscosity of the crust in the Sichuan Basin would need to be greater
411 than $\sim 4 \times 10^{24}$ Pas to remain undeformed by horizontal forces associated with gravitational
412 potential energy contrasts. The viscosity required would be lower if the topographic contrast
413 were supported for a shorter time. We can test whether this viscosity is reasonable using
414 laboratory-derived flow laws. We use the dry flow laws for typical lower crustal minerals
415 from Bystricky and Mackwell (2001) and Rybacki et al. (2006), and calculate the tempera-
416 ture corresponding to a viscosity of 4×10^{24} Pas at the Moho (36–40 km, Liu et al., 2014),
417 assuming lithostatic pressure and a grain size of 1 mm. For both flow laws, the viscosity
418 will be $\geq 4 \times 10^{24}$ Pas if the temperature is less than ~ 800 – 900°C . Moho temperatures in

419 undeforming Precambrian crust are typically $\sim 600^\circ\text{C}$ (McKenzie et al., 2005), meaning that
420 the viscosity required for the Sichuan Basin to behave rigidly on the timescales of our model
421 is consistent with laboratory-derived flows laws. Rather than adding additional parameters
422 to our model describing the rheology of the lower crust in the basins, we simply model the
423 lower crust in the basins as rigid. As discussed in section 1, the geological structure of the
424 Central Myanmar Basin is less well constrained than that of the Sichuan Basin, but it also
425 acts in a rigid manner, so for simplicity we make the same assumption there.

426

427 Outside the basins, the base of the current in our models is stress-free (meaning that
428 vertical derivatives of horizontal velocities are zero at the base of the current; England and
429 McKenzie, 1982, 1983; Copley and McKenzie, 2007), implying that the asthenosphere im-
430 poses negligible shear stress on the base of the lithosphere. Since we only model the deforma-
431 tion of the crust, we are assuming that the crust and lithospheric mantle deform coherently
432 in the region with the stress-free base, and that shearing over the lithospheric mantle plays
433 a limited role in the force balance of the lower crust. For this assumption to hold true, the
434 lithospheric mantle should have a sufficiently low viscosity that dominant stress driving its
435 motion is the deviatoric stress resulting from flow in the lower crust, rather than the stress
436 imposed on vertical planes by shearing past the basins. From our modelling, the deviatoric
437 strain rate in the centre of the inter-basin region is $\sim 5 \times 10^{-16}\text{s}^{-1}$, giving a deviatoric stress
438 of 10 MPa in the lower crust, using a crustal viscosity of 10^{22} Pas. The shear strain rate on
439 the basin margins is $\sim 3 \times 10^{-15}\text{s}^{-1}$. For our assumption to hold, therefore, the viscosity of
440 the lithospheric mantle should be $\ll 10^{21}$ Pas. Using the flow laws derived for wet olivine
441 by Hirth and Kohlstedt (2003) with a grain size of 1 mm, 1.5 GPa pressure (lithostatic
442 pressure at the Moho beneath ~ 55 km thick crust), 1 GPa water fugacity, and a strain rate
443 of 10^{-16}s^{-1} , effective viscosities less than 10^{21} Pas correspond to temperatures above ~ 400 –
444 700°C (depending on whether deformation occurs by dislocation or diffusion creep). Effective

445 viscosities less than 10^{19} Pas, such that the shear stress imposed on the lithospheric mantle
446 at the basin margins would be two orders of magnitude less than the principal deviatoric
447 stress in the lower crust, correspond to temperatures above $\sim 800^\circ\text{C}$. These temperatures
448 are consistent with temperature estimates from lithospheric mantle xenoliths in south-east
449 Tibet (Yu et al., 2010; Liu et al., 2013), suggesting that modelling crustal deformation with a
450 stress-free base outside the basin regions is reasonable. Copley (2008) also demonstrated the
451 possibility of coherent lower crust and lithospheric mantle deformation in south-east Tibet
452 using rheologies extrapolated from laboratory flow laws. Although such extrapolations lead
453 to vertical gradients in viscosity, in many cases these gradients, and the length-scales over
454 which they occur, are insufficient to result in appreciable contrasts in horizontal velocities.

455

456 The top surface of the current in our models is stress-free throughout the model domain,
457 representing the lack of significant tractions imposed by the atmosphere. We track particles
458 on this surface, which move with the horizontal velocity at their location at each time step.
459 These particles are analogous to the samples used in palaeoaltimetric studies.

460

461 In some models we investigate the interaction between erosion and propagation of the
462 current by incorporating an erosive term;

$$\frac{\partial s}{\partial t} = -\kappa |\nabla s|, \quad (1)$$

463 where κ is a constant. Gradient-dependent erosion is suggested by higher erosion rates and
464 greater cumulative erosion in the Longmen Shan than in the interior of the Sichuan Basin
465 and Tibetan Plateau (Richardson et al., 2008). This erosive term has the same derivation as
466 the classic Culling model (Culling, 1960), but assumes that eroded material is removed from
467 the model domain. This assumption is consistent with Hubbard et al.'s (2010) proposal that

468 sediment is transported away from the Sichuan basin by the Yangtze River.

469

470 **3.3 Lateral Boundary Conditions**

471 The mathematical details of the lateral boundary conditions we use in our models are given
472 in Appendix A. Here we summarise these boundary conditions and explain their physical
473 motivation. The intention of these models is to investigate the effects of variations in the
474 strength of the lower crust on the temporal evolution of topography. In South East Tibet,
475 this evolution is likely to be driven by gravitational potential energy contrasts (see Sec-
476 tion 3.2 above), so the aim of these boundary conditions is to approximate the features of
477 South East Tibet which lead to, and control, the topographic evolution: high topography
478 and thick crust in the Tibetan Plateau, and thinner crust to the south-east. The boundary
479 conditions we adopt are symmetric, and do not vary in the x ('east-west') direction, so 'east-
480 west' variations in the development of topography in our model must result from the lateral
481 changes in basal boundary conditions.

482

483 Initially ($t = 0$), the domain is filled with a 40 km-thick layer of fluid (H_0 , Figure 4),
484 chosen to represent generic, undeformed continental crust. There may have been pre-existing
485 topography in south-east Tibet before the onset of Cenozoic deformation (Burchfiel et al.,
486 1995; Hubbard et al., 2010). However, the shape of this topography is poorly constrained,
487 so we assume an initially flat, uniform layer for simplicity.

488

489 At one edge of the model domain ($y = 0$) fluid flows into the region, analogous to the
490 lateral growth of a mountain range, in this case from central Tibet into south-east Tibet.
491 The topography along this boundary is 4.5 km above the surface of the 40 km thick layer in
492 the remainder of the model domain, similar to the mean elevation of the Tibetan Plateau

493 above the Sichuan Basin (Figure 1). This elevation contrast, combined with our assumption
494 of Airy isostasy, corresponds to a crustal thickness at the input boundary of 65 km, similar
495 to that beneath the Tibetan Plateau (e.g. Liu et al., 2014). The height of the topography
496 on this boundary is kept constant throughout the model evolution. Using a fixed-height
497 boundary condition is analogous to assuming that the central Tibetan plateau has been at
498 its present elevation throughout the development of high topography in south-east Tibet.
499 This simple assumption allows us to isolate the effects of lateral variations in lower-crustal
500 strength in south-east Tibet, and is consistent with palaeoaltimetric data, which suggest that
501 the central plateau has been high since at least the Eocene (e.g. Rowley and Currie, 2006).
502 We assume zero deviatoric stress normal to this influx boundary ($\sigma'_{yy} = 0$), equivalent to a
503 reservoir of high material at the edge of the model domain (i.e. the central Tibetan Plateau),
504 which can supply fluid to the current at the same rate at which fluid moves away from the
505 boundary (Figure 4, Appendix A; Reynolds et al., 2015). We set the velocity parallel to this
506 boundary to zero ($u = 0$ on $y = 0$), motivated by the small velocity component parallel to
507 the NW boundary of Figure 3. The starting topography within the model domain adjacent
508 to this influx boundary has a constant slope in the y direction (Figure 4); its gradient does
509 not affect the model results after the first few timesteps.

510

511 At the ‘southern’ end of the domain as shown in Figure 4 ($y = y_{max}$), and beyond the
512 basins ($y > y_b$), we assume that there is an external reservoir of 40 km thick crust, which
513 does not deform in response to the evolution of topography inside the model domain. We
514 set the derivatives of the horizontal velocities in the direction perpendicular to these bound-
515 aries to zero (i.e. $\frac{\partial v}{\partial y} = \frac{\partial u}{\partial y} = 0$ on $y = y_{max}$, and $\frac{\partial u}{\partial x} = \frac{\partial v}{\partial x} = 0$ on $x = 0$ and $x = x_{max}$).
516 These conditions correspond to zero deviatoric normal stress acting perpendicular to these
517 boundaries, and boundary-parallel velocities not contributing to the shear stress on these
518 boundaries. These boundary conditions are equivalent to there being no deviatoric stresses

519 being imposed on the model domain by the material outside it, and are consistent with
520 the lack of significant faulting, low earthquake- and GPS-derived strain rates, and uniform,
521 $\sim 35\text{--}40$ km crustal thicknesses (Xu et al., 2013) outside the region of south-east Tibet which
522 corresponds to our model domain (Figure 3).

523

524 Along $x = 0$ and $x = x_{max}$ we use a reflection boundary condition up to the end of the
525 basins ($y < y_b$). This is equivalent to assuming that mountains also exist to either side of
526 the model domain, and are behaving in the same manner in these regions; analogous to high
527 topography existing to the north of the Sichuan Basin and the Central Lowlands of Myanmar.

528

529 **4 Results & Comparison to South East Tibet**

530 We initially use symmetric models (i.e. where the two basins with strong lower crust have
531 the same size and are the same distance from the influx boundary) to investigate the effects
532 of changing basal thickness and inter-basin width (defined in Figure 4) on the evolution of
533 topography. Figure 5 shows the results of a model with symmetric basins of radius 450 km
534 (grey semi-circles, Figure 5c, equivalent to an inter-basin width of 600 km), and basal thick-
535 ness 15 km. Times referred to are since the start of the model and elevations are given
536 relative to the surface of 40 km-thick, isostatically-compensated crust. As discussed in Sec-
537 tion 3, the velocity and, therefore, the rate of topographic evolution, are expected to scale
538 linearly with the viscosity. We therefore expect that the topography after 50 Myr of model
539 evolution with a viscosity of 10^{22} Pas (as shown in Figure 5a) would correspond to that after
540 5 Myr for a viscosity of 10^{21} Pas.

541

542 Regions with a stress-free base develop gentle topographic gradients (< 0.004 , in contrast

543 to gradients of ~ 0.02 on the margins of the basin regions, which are discussed below). De-
544 formation in these regions is effectively by pure shear of vertical planes; relatively gentle
545 topographic gradients result from the quasi-depth-independent horizontal velocities. Sim-
546 ilar, gentle topographic gradients are also a feature of thin-viscous-sheet models (England
547 and McKenzie, 1982, 1983, even where these models use high stress-exponents; Section 3.1),
548 which have the same, stress-free, basal boundary condition. The topographic gradients in
549 the stress-free regions are very similar in magnitude to the south-eastwards topographic gra-
550 dients in the high region between the Sichuan Basin and the Central Lowlands of Myanmar
551 (compare Figures 6h and 6f – the topographic profile location is shown in Figure 2a). We
552 expect these gradients to be partially controlled by the location of the model boundaries
553 which, as discussed in Section 3.3, are consistent with the deformation and crustal thick-
554 nesses in south-east Tibet.

555

556 In contrast to regions with a stress-free base, steep topographic gradients develop in the
557 basin regions, suggesting that steep topography can form as a result of mountain ranges over-
558 riding rigid lower crust. The development of very different topographic gradients in regions
559 with and without a rigid base (compare Figures 6a, c and e to Figures 6b, d and f), therefore,
560 shows the first-order control exerted by the basin regions on the shape of the topography.
561 These different topographic gradients are consistent with previous work showing that flow
562 over a rigid base results in steeper gradients than flow over a stress-free base (e.g. McKenzie
563 et al., 2000).

564

565 The topography also propagates more slowly in the basin regions than in the region be-
566 tween them (compare Figure 6 c and d). Where flow occurs over a rigid base, the velocity
567 depends on the square of the flow depth (Huppert, 1982). Increasing the basal thickness
568 (analogous to having a thicker rigid lower crust or a thinner overlying layer of deformable

569 rock) therefore, reduces the distance which the current propagates into the basin in a given
570 time, and also results in steeper topographic profiles where the flow overrides the basin. This
571 effect is demonstrated by Figure 6, which shows profiles through models with the same basin
572 locations as in Figure 5, but with varying basal thicknesses. Figures 6 a & b, c & d and e &
573 f have basal thicknesses of 0 km (only the base is rigid), 15 km and 30 km respectively. A
574 proportionally thicker rigid region (e.g. Figure 6e) means that the current is flowing into a
575 thinner fluid layer, so tends to develop a sharper nose, as shown by McKenzie et al. (2000).
576 The topographic gradients across the Longmen Shan (Figures 6g) are very similar to those
577 in our model for a basal thickness of 30 km (corresponding to 10 km initial thickness of
578 deformable rock in the basin regions). This basal thickness is consistent with ~ 10 km of
579 sediment overlying Paleoproterozoic basement in the Sichuan Basin (Hubbard and Shaw,
580 2009).

581

582 Erosion also leads to steeper topographic gradients, and hinders current propagation in
583 the basins. The dashed lines in Figure 6c and d show the results of eroding the topography
584 with $\kappa = 4 \text{ mm yr}^{-1}$ in equation (1). The erosive term we use is proportional to gradient
585 (Section 3), meaning that the steep slopes in the basins are affected more than gentle slopes
586 in the inter-basin region (compare dashed lines in Figures 6c and d). With $\kappa = 4 \text{ mm yr}^{-1}$ the
587 topography is quasi-stationary on the basin margins between 15 and 50 Myr (dashed blue
588 and red lines in Figure 6c), demonstrating that erosion can stop the propagation of topog-
589 raphy in these regions (equivalent to the suggestion of Koons, 1989, for the South Island of
590 New Zealand), but not in the region of fast flow between the basins. The similar position of
591 the present-day Longmen Shan and the Paleogene deformation front adjacent to the Sichuan
592 Basin (derived from stratigraphic thicknesses of foreland basin sediments; Richardson et al.,
593 2008) could, therefore, result from erosion acting on topography which would otherwise be
594 propagating over the basin. Such an effect is possible because of the slow propagation of

595 topography over rigid lower crust.

596

597 The distance between basins controls the velocity of the current in the region between
598 them. Figure 7 shows the topographic and velocity profiles resulting from different inter-
599 basin widths, with constant basal thickness (15 km). Greater inter-basin widths result in
600 faster velocities perpendicular to the profile (v , Figures 7b, d, f). Flow in the inter-basin
601 region is dominated by simple shear of horizontal planes – similar to that between two rigid
602 walls (as suggested by Copley and McKenzie, 2007), with maximum velocity proportional to
603 width squared. The width of the rapidly deforming region between the Sichuan Basin and
604 the Central Lowlands of Myanmar is ~ 500 km. Observed GPS velocities relative to Eurasia
605 in the centre of this region are ~ 20 mm yr $^{-1}$. Inter-basin velocities in our model are similar
606 to these GPS velocities for an inter-basin width of 600 km, which suggests that the viscosity
607 we use for our modelling (10^{22} Pas) is reasonable.

608

609 As discussed in section 3.2, our models do not include flexural support of the topography.
610 If we did include flexural support we would not expect to see qualitatively different topog-
611 raphy, because the wavelengths associated with such support are small in comparison to the
612 scale of our model. Viscous models of the crust, such as the one we use here, implicitly inves-
613 tigate long wavelength deformation, at scales longer than individual faults (Figure 3, England
614 and McKenzie, 1982, 1983). Gravity anomalies demonstrate flexural effects in south-east Ti-
615 bet acting on wavelengths less than ~ 50 km (Fielding and McKenzie, 2012), and isostatic
616 compensation throughout the region of high topography (Jordan and Watts, 2005; Fielding
617 and McKenzie, 2012). Specifically, Fielding and McKenzie (2012) found a lower bound on
618 the elastic thickness of the Sichuan Basin of 10 km (although this value is poorly constrained
619 since the basin is too small for the full flexural wavelength to be measured) and an elastic
620 thickness of 7 km for the adjacent high topography. Flexure may provide local support to

621 the topography where it overthrusts the Sichuan Basin (in our model, over the horizontally
622 rigid basin). The topographic gradient in this region of our model, therefore, represents an
623 end-member in which the rigid (zero horizontal velocity) base is free to move vertically. The
624 other end-member, in which the base cannot move vertically in response to being loaded,
625 also leads to steep fronts (Huppert, 1982). The rigid nature of the basal boundary (i.e. the
626 no-slip condition on the base of the fluid) controls the shape of the topography, rather than
627 whether or not this boundary is able to deform vertically (McKenzie et al., 2000). Ball et al.
628 (2019) demonstrated that flexural effects are primarily important near the nose of a viscous
629 current, but that such currents over a flexed base can still form steep topographic gradients
630 provided the base of the current has a no-slip boundary condition. The difference in basal
631 boundaries conditions, and the depth of deformable rock, therefore, provide a first-order
632 explanation for contrasting topographic gradients in south-east Tibet, even if our models do
633 not capture the precise, short-wavelength details of flexural effects on the topography.

634

635 The elevation histories of particles we track at the surface of the current (Figure 5d) show
636 that uplift rates from our model are $\sim 0.1\text{--}0.5\text{ mm yr}^{-1}$ in the centre of the inter-basin region
637 (red star in Figure 5d), similar to the $< 0.3\text{ mm yr}^{-1}$ uplift rates derived from palaeoal-
638 timetry (Section 2, Figure 2). The highest uplift rates in our model ($\sim 0.5\text{ mm yr}^{-1}$, green
639 diamond) occur within the first 10–15 Myr of model evolution for particles moving into the
640 inter-basin region. These rates and locations are similar to those in the only region (region
641 1, the Gonjo basin, Figure 2) where uplift rates $> 0.3\text{ mm yr}^{-1}$ have been suggested from
642 palaeoaltimetry in South East Tibet. However, our modelling also demonstrates that the
643 interpretation of palaeoelevation results is not straightforward. Figure 5 shows that ma-
644 terial at the surface may be transported long distances (hundreds of kilometres over tens
645 of millions of years for the viscosity used here). The advection of particles with the flow
646 means that elevation histories may be complex, with particle elevations decreasing “south”

647 (towards $y = y_{max}$) of the inter-basin region as the current spreads laterally (the same effect
648 which leads to the extensional strain rates described below). Pedogenic carbonates which
649 are found to have been high in the late Eocene–early Miocene (Hoke et al., 2014; Li et al.,
650 2015; Gourbet et al., 2017) could have been deposited at similar latitudes to samples from
651 the Longmen Shan, which were at their present elevation in the late Miocene (Xu et al., 2016).

652

653 By considering the principal axes of the horizontal strain-rate tensor at the surface of
654 our model (Figure 5b) as analogous to the strain rate in the brittle crust (Houseman and
655 England, 1986), we can draw comparisons between our model and the geodetic and seismic
656 strain rates in south-east Tibet. The largest strain-rates in both our model and in south-east
657 Tibet are associated with shear at the basin margins. Strain rates equivalent to left-lateral
658 shear adjacent to Basin E (Figure 4), and right-lateral shear adjacent to Basin W (Figure 4)
659 are analogous to left-lateral slip on the Xianshuihe Fault and right-lateral slip on the Nui-
660 jiang and Sagaing Faults (and adjacent, rotating, left-lateral faults) respectively.

661

662 Where steep topography forms along the ‘northern’ edges of the basin, the principal com-
663 pressional axes of the horizontal strain rate tensor are approximately perpendicular to the
664 basin margins. These compressional strain rates are small in comparison to the shear strain
665 rates where the flow is sub-parallel to the basin margins. In the context of south-east Tibet,
666 this suggests that the steep topography and low shortening rates across the Longmen Shan
667 could result from flow of weaker material over the rigid lower crust of the Sichuan Basin
668 (Copley, 2008; Fielding and McKenzie, 2012), without a low-viscosity, lower-crustal channel.

669

670 The principal axes of the horizontal strain-rate tensor at the surface of our models show
671 two extension-dominated regions (red ellipses in Figure 5b), with similar locations and ori-
672 entations to the normal faulting in south-east Tibet (red ellipses and focal mechanisms in

673 Figure 1b). The extensional strain rates in these parts of our model are ~ 2 –5 times larger
674 than the compressional strain rates, so these regions are equivalent to mixed strike-slip and
675 normal faulting, with normal faulting dominating. Extension in the y direction ‘north’ of the
676 basins (top white ellipse in Figure 5b) is comparable to the northern group of normal faults
677 in Figure 1, which accommodate extension parallel to the topographic gradient (striking
678 perpendicular to both topographic gradients and GPS velocities relative to Eurasia, Fig-
679 ure 3). Our modelling suggests that this extension may result from a velocity increase where
680 the topography flows through the inter-basin region. The second region of extension occurs
681 where fluid spreads out laterally to the ‘south’ of the basins; increasing the surface area of
682 the current. This extension perpendicular to topographic gradients is shown by the bottom
683 white ellipse in Figure 5b. The southern group of normal faults shown in Figure 1 also
684 accommodate extension perpendicular to the topographic gradients.

685

686 Figure 8 shows the results of changing the shape of one of the basins to be more similar
687 to that of the Central Lowlands of Myanmar. The region of shear which develops adjacent
688 to this basin extends further ‘south’ than that adjacent to a semi-circular basin. We expect
689 that this larger region of shear develops because the flow is approximately parallel to the
690 change in basal boundary condition over a longer distance than when the basin is semi-
691 circular. This region of shear is similar to the area of distributed left-lateral faulting east of
692 the Sagaing fault (Figure 1a), which accommodates right-lateral shear through vertical-axis
693 rotations (Copley, 2008). The lateral extent of this shear in south-east Tibet may, therefore,
694 be controlled by the geometry of the rigid lower crust in the Central Lowlands of Myanmar.

695

5 Discussion

Our model, considering the effect of lateral lower crustal strength variations consistent with geophysical and geological observations, allows us to reproduce the main features of the present-day topography, strain-rate and velocity field in south-east Tibet, and uplift rates from palaeoaltimetry. These results demonstrate that lateral strength contrasts, in the form of regions of rigid lower crust, provide a first-order control on the temporal evolution of mountain ranges (Figure 9). Below we discuss our key findings and their application to mountain ranges in general.

In our model, which has mechanically-coupled upper and lower crust, surface uplift rates are $< \sim 0.5 \text{ mm yr}^{-1}$. These gradual uplift rates are consistent with palaeoaltimetry results in south-east Tibet, suggesting that no low-viscosity, lower-crustal channel is required to explain the evolution of topography in this region. However, our modelling also suggests a potential caveat in the interpretation of paleoaltimetry results. Particle tracking in our models shows that material at the surface where the crust flows over a stress-free base may be transported long distances (hundreds of kilometres over millions of years for the viscosity used here). Calculated palaeoelevations, therefore, estimate the palaeoelevation of the place where the sample was deposited, rather than the palaeoelevation of its present-day location. Accounting for this lateral transport is also important for converting the oxygen-isotope composition of carbonates to palaeoelevation, potentially requiring greater continentality corrections.

Our modelling demonstrates that differences in basal boundary condition, analogous to the presence or absence of strong lower crust, can lead to the development of contrasting topographic gradients. In particular, steep gradients arise naturally from flow over a rigid

721 (no-slip) base. The present-day, compressional strain rates perpendicular to these steep mar-
722 gins are small in comparison to the horizontal shear strain rates where deformation is parallel
723 to the basin margins in both our model (Figures 5 and 8), and in south-east Tibet (Figures 1
724 and 3 Shen et al., 2005; Zheng et al., 2017). This combination, of steep-fronted topography
725 and low compressional strain rates, is a feature of other parts of the India-Eurasia collision.
726 Steep topographic gradients on the northern margin of the Tibetan Plateau, adjacent to the
727 Tarim basin (~ 3 km over 50 km), and the low rate of shortening ($0\text{--}3$ mm yr $^{-1}$, e.g. Zheng
728 et al., 2017) across the basin margin, are similar to those in the Longmen Shan. Increasing
729 Moho depths from north to south across the margin (Wittlinger et al., 2004), and the flex-
730 ural signal seen in free-air gravity anomalies (e.g. McKenzie et al., 2019), suggests that the
731 western edge of the Tarim Basin may underthrust the western Kunlun ranges, which would
732 provide a rigid base to the flow of crustal material from northern Tibet, in a similar manner
733 to the Sichuan Basin in south-east Tibet. The temporal evolution of topography adjacent
734 to the Tarim Basin may, therefore, also be controlled by the lateral strength contrast be-
735 tween rigid lower crust in the Tarim Basin and lower viscosity crust in Tibet. The motion of
736 southern Tibet over rigid India is likely to represent the same effect. However, the rates of
737 motion in southern Tibet are more rapid than in northern Tibet, perhaps due to differences
738 in the thicknesses, temperatures or compositions of the crust in India and the Tarim basin
739 (McKenzie et al., 2019).

740

741 More generally, the control on topographic evolution provided by lateral strength con-
742 trasts, particularly the low rates of propagation of topography into regions with rigid lower
743 crust (Figures 6, 9), suggests an explanation for the correlation of cratonic regions with steep
744 edges of mountain belts (including the Atlas mountains, the Caucasus and older orogenies
745 such as the Appalachians in North America) noted by McKenzie and Priestley (2008). Cra-
746 tonic regions are likely to have relatively strong lower crust (e.g. Jackson et al., 2008), so

747 our results suggest that the propagation of topography into these regions will be slow in
748 comparison to adjacent regions where the lower crust has lower viscosity.

749

750 We also find that the thickness of strong lower crust, and of deformable material (such as
751 sediments) above it, controls the extent of mountain range propagation and the morphology
752 of the range front. Larger thicknesses of deformable rock (fluid layer above the rigid base
753 in our models) lead to more rapid propagation of topography over regions with strong lower
754 crust, and to shallower topographic gradients. This result is likely to apply to mountain
755 ranges globally. The occurrence of thin-skinned deformation of sediments above the edge of
756 the South American craton, in the foothills of the Eastern Cordillera of the Andes (Lamb,
757 2000), suggests that the deformation in this region is comparable to flow over a rigid base.
758 The foothills in the southern Bolivian Andes extend further east than those in the north, and
759 have lower topographic gradients. This broader foothill region correlates with higher sedi-
760 ment thicknesses in the bounding basin (McGroder et al., 2014), similar to the current in our
761 model propagating further over a rigid base where the deformable layer is thicker (Figure 6c
762 and e). Wimpenny et al. (2018) suggested that this effect might lead to the onset of extension
763 in the adjacent mountains. Along-strike variations in sediment thickness can also explain
764 variations in the morphology of the Indo-Burman Ranges (Ball et al., 2019), although there
765 mountain building is driven by the subducting plate, which advects sediment laterally, as
766 well as by contrasts in gravitational potential energy. Ball et al. (2019) highlighted that it is
767 the thickness of deformable sediment, rather than the total sediment thickness, which is im-
768 portant in controlling morphology. Although beyond the scope of this study, we expect that
769 along-strike variations in the viscosity of the deformable rock, as well as its thickness, could
770 lead to similar changes in morphology. In the Zagros mountains, for example, along-strike
771 variations in the width of high topography could potentially correlate with the presence or
772 absence of weak salt layers (Nissen et al., 2011). Similarly, the prominent curvature of the

773 Sulaiman Ranges, and their projection beyond the general ~north–south strike of the Pak-
774 istan range front, has been proposed to result from a package of weak sediments beneath
775 them (Reynolds et al., 2015).

776

777 For crust in south-east Tibet, it is not clear whether ductile deformation is dominated by
778 diffusion creep, which is Newtonian with a stress exponent of 1, or dislocation creep, which
779 has a power-law rheology with a stress exponent greater than 1 (e.g. Stocker and Ashby,
780 1973). In our modelling, we have, therefore, taken the simplest approach, which is to use a
781 Newtonian rheology with a constant viscosity. Our models show that such a rheology can pro-
782 duce steep topographic gradients where flow occurs over a rigid base, such as strong lower
783 crust. In contrast, in models where depth variations in horizontal velocity are neglected,
784 steep topographic gradients require a power-law rheology with a high stress exponent, and,
785 even then, these gradients are much shallower than those in the Longmen Shan (Section 3.1,
786 Houseman and England, 1986; England and Houseman, 1986; Lechmann et al., 2011). If
787 dislocation creep does control ductile deformation, the vertically-integrated strength of the
788 lithosphere can be represented as a single power-law rheology (Sonder and England, 1986).
789 An interesting question, therefore, is whether the steep topographic gradients in our model
790 would still form if we had used a power-law, rather than a Newtonian, rheology. A higher
791 stress-exponent would tend to localise deformation in regions of high strain rate, such as im-
792 mediately above the rigid lower crust in the basin regions. The second invariant of the strain
793 rate tensor in these regions of our model is $\sim 10^{-15} \text{ s}^{-1}$, consistent with geodetically- and
794 geologically-estimated strain rates in tectonically active regions (Fagereng and Biggs, 2019).
795 For a viscosity of 10^{22} Pas this strain rate corresponds to a stress of $\sim 10 \text{ MPa}$, typical of
796 earthquake stress drops (Kanamori and Anderson, 1975; Allmann and Shearer, 2009). If the
797 crust were to deform with a power-law rheology with a stress-exponent of 3, and assuming a
798 strain rate in the rest of the model domain of $\sim 10^{-16} \text{ s}^{-1}$, these strain rates would lead to

799 a local drop in viscosity from 10^{22} Pas to $\sim 2 \times 10^{21}$ Pas, which might lubricate the base of
800 the current. However, the flow over the rigid base would still be much slower than that with
801 a stress-free base, and have a non-linear dependence on the thickness of the current, mean-
802 ing that we would still expect contrasting topographic gradients to develop. Mathematical
803 studies of gravity currents composed of power-law fluids suggest that, although there may
804 be some increase in far-field surface slope associated with such effects, flow over a rigid base
805 nonetheless tends to produce a steep front (Gratton et al., 1999). Our result, that steep
806 topographic gradients can form with a Newtonian rheology, therefore, suggests that steep-
807 fronted mountain ranges do not constrain whether flow in the ductile part of the lithosphere
808 occurs by diffusion or dislocation creep, but demonstrate the governing role of lower crustal
809 strength in determining the topographic gradients of mountain ranges.

810

811 **6 Conclusion**

812 We have investigated the role of lateral contrasts in lower crustal strength in controlling
813 the shape and evolution of mountain ranges. In south-east Tibet, stable-isotope palaeoal-
814 timetry suggests that parts of the topography may have been at, or near, their present-day
815 elevations since the late Eocene and that uplift is likely to have occurred more slowly than
816 had previously been inferred. In combination with a simple model, these palaeoaltimetry
817 results demonstrate that lateral strength contrasts are sufficient to explain first-order fea-
818 tures of the deformation and topographic evolution in south-east Tibet, without invoking a
819 low-viscosity, lower-crustal channel. Since our models of topographic evolution in the pres-
820 ence of lateral lower-crustal strength contrasts allow us to reproduce the main features of
821 the present day topography, strain-rate and velocity field in south-east Tibet, we suggest
822 that lateral strength contrasts provide a first-order control on the temporal evolution and

823 shape of mountain ranges. Our modelling also suggests that lateral contrasts in lower crustal
824 strength provide an explanation for the correlation between cratons and the steep gradients
825 on the edges of some mountain ranges.

826 **Acknowledgements**

827 C.P. would like to thank Thomasina Ball and Jerome Neufeld for helpful discussions. We
828 also thank Sergei Medvedev and an anonymous reviewer for their detailed comments. This
829 work forms part of the NERC- and ESRC-funded project ‘Earthquakes without Frontiers’
830 and was partially supported by the NERC large grant ‘Looking inside the Continents from
831 Space’. C.P. is funded by a Junior Research Fellowship from Queens’ College, University of
832 Cambridge and was funded by a NERC studentship for part of the research. Figures were
833 prepared using the GMT package (Wessel et al., 2013).

834 **Data and code**

835 No data was created for this research. Palaeoaltimetry data can be found in Hoke et al.
836 (2014); Li et al. (2015); Xu et al. (2016); Tang et al. (2017); Gourbet et al. (2017); Wu
837 et al. (2018). Earthquake focal mechanisms can be found in Copley (2008) (and references
838 therein), Zhang et al. (2010), Li et al. (2011), Han et al. (2014), Bai et al. (2017), Han et al.
839 (2018), the CMT catalogue (Dziewonski et al., 1981; Ekström et al., 2012) and the ISC-
840 EHB catalogue (Engdahl et al., 1998; International Seismological Centre, 2016). GPS data
841 in Figure 3 are from Zheng et al. (2017). The code used to produce the modelling results
842 shown in Figures 5, 6, 7, 8 can be found on Zenodo, <https://doi.org/10.5281/zenodo.4090916>

843 .

844 **A Time evolution of a viscous current**

We solve a simplified form of the Stokes' flow equations, proposed by Pattyn (2003) for glaciers. This form of the governing equations makes two main assumptions about the vertically-oriented stresses, $\sigma_{nz} = \eta \left(\frac{\partial w}{\partial n} + \frac{\partial u_n}{\partial z} \right)$, where $n \in \{x, y\}$ represents either horizontal direction, based on scaling analysis (Pattyn, 2003). The first assumption is that lateral variations of these stresses are small in comparison to the increase in lithostatic pressure with depth, such that the vertical normal stress is given by the lithostatic pressure:

$$\sigma_{zz} = P_l = \int_z^s \rho g dz'. \quad (\text{A.1})$$

845 The second assumption is that the vertical derivatives $\frac{\partial \sigma_{nz}}{\partial z}$, can be neglected in the horizon-
 846 tal momentum balance, except in parts of the domain with no-slip boundary conditions (and
 847 immediately adjacent areas; Pattyn, 2003; Schmalholz et al., 2014). In these areas, vertical
 848 gradients in horizontal velocities, $\frac{\partial u_n}{\partial z}$, are important. The vertically-oriented stresses are,
 849 therefore, simplified everywhere to $\sigma_{nz} = \eta \left(\frac{\partial u_n}{\partial z} \right)$, $n \in \{x, y\}$. These assumptions do not
 850 imply that the vertical velocities cannot vary horizontally, only that the terms $\frac{\partial w}{\partial n}$ do not
 851 dominate the balance of forces driving the flow.

852

853 We follow Pattyn in scaling the vertical dimension at each timestep (cf. his equation
 854 44). We then solve the resulting velocity equations at each timestep (subject to the bound-
 855 ary conditions discussed below and in section 3.3) using the generalised minimum residual
 856 method (Saad and Schultz, 1986, in sparskit2).

857

858 At each timestep we first solve for the horizontal velocities, then calculate the associated
 859 evolution of the topography. From integrating the incompressibility condition, $\frac{\partial u}{\partial x} + \frac{\partial v}{\partial y} + \frac{\partial w}{\partial z} =$

860 0, over the layer thickness, H (Figure 4):

$$\frac{\partial H}{\partial t} = -\nabla_h \cdot (H\bar{u}, H\bar{v}), \quad (\text{A.2})$$

861 where bars denote vertical averaging, and

$$\nabla_h = \left(\frac{\partial}{\partial x}, \frac{\partial}{\partial y} \right). \quad (\text{A.3})$$

862 Equation (A.2) can be written as a diffusion equation for the topography. This approach
 863 allows the diffusivities to be calculated on a staggered grid, preventing leapfrog instabilities
 864 in the second-order finite differences. Pattyn (2003) expressed this diffusion equation as:

$$\frac{\partial H}{\partial t} = \nabla_h \cdot \left(D_x \frac{\partial H}{\partial x}, D_y \frac{\partial H}{\partial y} \right) + \nabla_h \cdot \left(D_x \frac{\partial b}{\partial x}, D_y \frac{\partial b}{\partial y} \right), \quad (\text{A.4})$$

(his equation 55, where we make the derivatives explicit here for clarity), and:

$$D_x = \left| \bar{u} H \left(\frac{\partial s}{\partial x} \right)^{-1} \right|,$$

$$D_y = \left| \bar{v} H \left(\frac{\partial s}{\partial y} \right)^{-1} \right|,$$

(the modulus signs were implied but not included in Pattyn, 2003). In the glacier case, for which this method was developed, there is no prescribed relationship between the surface height, s , and bed depth, b (although $H = s - b$). However, for an Airy isostatically-compensated fluid, such as the crust of south-east Tibet (e.g. Jordan and Watts, 2005), $b = -fs$ and $H = (1 + f)s$, where $f = \frac{\rho_c}{\rho_m - \rho_c}$. For standard crust and mantle densities of 2700 kg m^{-3} and 3300 kg m^{-3} respectively, $f = 4.5$, which is what we assume here.

Substituting these relationships into (A.4) gives

$$\frac{\partial H}{\partial t} = \left(\frac{1}{f+1} \right) \left(\frac{\partial}{\partial x} \left(D_x \frac{\partial H}{\partial x} \right) + \frac{\partial}{\partial y} \left(D_y \frac{\partial H}{\partial y} \right) \right). \quad (\text{A.5})$$

865 $D_n, n \in \{x, y\}$ becomes infinite if $\frac{\partial s}{\partial n} = 0$, but physically the topography in such regions
 866 should not propagate (i.e. $\frac{\partial H}{\partial t} = 0$, since in regions of flat topography there are no gravi-
 867 tational potential energy contrasts to drive the flow). In such cases, therefore, we set $D_n = 0$.

868

869 We write equation (A.5) as a sparse matrix equation using a Crank-Nicolson scheme
 870 for the finite differences, with diffusivities calculated on a staggered grid, the approach
 871 suggested by Pattyn (2003). Solving both x and y terms in the same linear system, rather
 872 than separating the components, gives better stability but means that the matrix does not
 873 have a simple form (the separated case is tridiagonal, which was the form used by Reynolds
 874 et al., 2015). We therefore solve this sparse system using the generalised minimum residual
 875 method (Saad and Schultz, 1986).

876 Lateral Boundary Conditions

877 We use constant height boundary conditions on $y = 0$ ($H = 65$ km), where fluid enters the
 878 model domain, and ‘south’ of the basins ($H = 40$ km). For the velocity boundary conditions
 879 on these boundaries, we set the deviatoric normal stresses perpendicular these boundaries to
 880 0, i.e. $\sigma'_{yy} = 2\eta \frac{\partial v}{\partial y} = 0$ on $y = 0, y = y_{max}$ and $\sigma'_{xx} = 2\eta \frac{\partial u}{\partial x} = 0$ on $x = 0, x = x_{max}$ for $y > y_b$
 881 (where y_b denotes the ‘southern’ end of the basins, Figure 4). On the ‘southern’ boundaries
 882 we also impose no contribution to boundary-parallel shear stresses on vertical planes from
 883 boundary-parallel velocities, that is $\frac{\partial u}{\partial y} = 0$ on $y = y_{max}$ and $\frac{\partial v}{\partial x} = 0$ on $x = 0, x = x_{max}$ for
 884 $y > y_b$. For the influx boundary ($y = 0$) we also set $u = 0$.

885 On $x \in \{0, x_{max}\}$ we use reflection boundary conditions $u = 0, \frac{\partial v}{\partial x} = 0$ for $y < y_b$. We

886 impose $u = 0$ directly, and use these conditions, along with our assumption of constant
887 viscosity and $\frac{\partial v}{\partial x} = 0$ to simplify the governing equation for v and solve this equation in its
888 co-ordinate transformed form.

889 References

- 890 Allmann, B. P. and Shearer, P. M. (2009). Global variations of stress drop for moderate to
891 large earthquakes. *J. Geophys. Res. Solid Earth*, 114(1):1–22.
- 892 Artyushkov, E. V. (1973). Stresses in the lithosphere caused by crustal thickness inhomom-
893 geneities. *J. Geophys. Res.*, 78(32):7675–7708.
- 894 Bai, L., Li, G., Khan, N. G., Zhao, J., and Ding, L. (2017). Focal depths and mechanisms
895 of shallow earthquakes in the Himalayan-Tibetan region. *Gondwana Res.*, 41:390–399.
- 896 Ball, T. V., Penney, C. E., Neufeld, J. A., and Copley, A. C. (2019). Controls on the
897 geometry and evolution of thin-skinned fold-thrust belts, and applications to the Makran
898 accretionary prism and Indo–Burman Ranges. *Geophys. J. Int.*, 218(1):247–267.
- 899 Beaumont, C., Jamieson, R. A., Nguyen, M. H., and Lee, B. (2001). Himalayan tecton-
900 ics explained by extrusion of a low-viscosity crustal channel coupled to focused surface
901 denudation. *Nature*, 414(6865):738–742.
- 902 Bischoff, S. and Flesch, L. (2019). Impact of Lithospheric Strength Distribution on India-
903 Eurasia Deformation From 3-D Geodynamic Models. *J. Geophys. Res. Solid Earth*,
904 124(1):1084–1105.
- 905 Burchfiel, B. C., Royden, L. H., van der Hilst, R. D., Hager, B. H., Chen, Z., King, R. W.,
906 Li, C., Lü, J., Yao, H., and Kirby, E. (2008). A geological and geophysical context for the

- 907 Wenchuan earthquake of 12 May 2008, Sichuan, People's Republic of China. *GSA Today*,
908 18(7):4.
- 909 Burchfiel, B. C., Zhiliang, C., Yupinc, L., and Royden, L. H. (1995). Tectonics of the
910 Longmen Shan and Adjacent Regions, Central China. *Int. Geol. Rev.*, 37(8):661–735.
- 911 Bystricky, M. and Mackwell, S. (2001). Creep of dry clinopyroxene aggregates with defor-
912 mation in the dislocation creep. *J. Geophys. Res.*, 106:13443–13454.
- 913 Chen, L., Gerya, T., Zhang, Z., Zhu, G., Duretz, T., and Jacoby, W. R. (2013a). Numerical
914 modeling of eastern Tibetan-type margin: Influences of surface processes, lithospheric
915 structure and crustal rheology. *Gondwana Res.*, 24(3-4):1091–1107.
- 916 Chen, L., Gerya, T. V., Zhang, Z. J., Aitken, A., Li, Z. H., and Liang, X. F. (2013b). For-
917 mation mechanism of steep convergent intracontinental margins: Insights from numerical
918 modeling. *Geophys. Res. Lett.*, 40(10):2000–2005.
- 919 Clark, M. K., Bush, J. W. M., and Royden, L. H. (2005a). Dynamic topography produced
920 by lower crustal flow against rheological strength heterogeneities bordering the Tibetan
921 Plateau. *Geophys. J. Int.*, 162:575–590.
- 922 Clark, M. K., House, M. A., Royden, L. H., Whipple, K. X., Burchfiel, B. C., Zhang, X., and
923 Tang, W. (2005b). Late Cenozoic uplift of southeastern Tibet. *Geology*, 33(6):525–528.
- 924 Clark, M. K. and Royden, L. H. (2000). Topographic ooze: Building the eastern margin of
925 Tibet by lower crustal flow. *Geology*, 28(8):703.
- 926 Clark, M. K., Royden, L. H., Whipple, K. X., Burchfiel, B. C., Zhang, X., and Tang, W.
927 (2006). Use of a regional, relict landscape to measure vertical deformation of the eastern
928 Tibetan Plateau. *J. Geophys. Res. Earth Surf.*, 111:F03002.

- 929 Clark, M. K., Schoenbohm, L. M., Royden, L. H., Whipple, K. X., Burchfiel, B. C., Zhang,
930 X., Tang, W., Wang, E., and Chen, L. (2004). Surface uplift, tectonics, and erosion of
931 eastern Tibet from large-scale drainage patterns. *Tectonics*, 23:TC1006.
- 932 Cook, K. L. and Royden, L. H. (2008). The role of crustal strength variations in shaping
933 orogenic plateaus, with application to Tibet. *J. Geophys. Res. Solid Earth*, 113(8):1–18.
- 934 Copley, A. (2008). Kinematics and dynamics of the southeastern margin of the Tibetan
935 Plateau. *Geophys. J. Int.*, 174:1081–1100.
- 936 Copley, A., Avouac, J. P., and Royer, J. Y. (2010). India-Asia collision and the Cenozoic
937 slowdown of the Indian plate: Implications for the forces driving plate motions. *J. Geophys.
938 Res. Solid Earth*, 115(3):1–14.
- 939 Copley, A. and McKenzie, D. (2007). Models of crustal flow in the India-Asia collision zone.
940 *Geophys. J. Int.*, 169:683–698.
- 941 Culling, W. E. H. (1960). Analytical Theory of Erosion. *J. Geol.*, 68(3):336–344.
- 942 Dalmayrac, B. and Molnar, P. (1981). Parallel thrust and normal faulting in Peru and
943 constraints on the state of stress. *Earth Planet. Sci. Lett.*, 55:473–481.
- 944 Dayem, K. E., Houseman, G. A., and Molnar, P. (2009a). Localization of shear along a
945 lithospheric strength discontinuity: Application of a continuous deformation model to the
946 boundary between Tibet and the Tarim Basin. *Tectonics*, 28(3):1–15.
- 947 Dayem, K. E., Molnar, P., Clark, M. K., and Houseman, G. A. (2009b). Far-field lithospheric
948 deformation in Tibet during continental collision. *Tectonics*, 28(6):1–9.
- 949 Dziewonski, A. M., Chou, T., and Woodhouse, J. H. (1981). Determination of earthquake
950 source parameters from waveform data for studies of global and regional seismicity. *J.
951 Geophys. Res.*, 86(B4):2825–2852.

- 952 Ekström, G., Nettles, M., and Dziewoński, A. M. (2012). The global CMT project 2004-2010:
953 Centroid-moment tensors for 13,017 earthquakes. *Phys. Earth Planet. Inter.*, 200-201:1–9.
- 954 Engdahl, E. R., van der Hilst, R., and Buland, R. (1998). Global teleseismic earthquake
955 relocation with improved travel times and procedures for depth determination. *Bull.*
956 *Seismol. Soc. Am.*, 88(3):722–743.
- 957 England, P. and Houseman, G. (1985). Role of lithospheric strength heterogeneities in the
958 tectonics of Tibet and neighbouring regions. *Nature*, 315:297–301.
- 959 England, P. and Houseman, G. (1986). Finite strain calculations of continental deforma-
960 tion: 2. Comparison with the India-Asia Collision Zone. *J. Geophys. Res. Solid Earth*,
961 91(B3):3664–3676.
- 962 England, P. and McKenzie, D. (1982). A thin viscous sheet model for continental deforma-
963 tion. *Geophys. J. Int.*, 70:295–321.
- 964 England, P. and McKenzie, D. (1983). Correction to: a thin viscous sheet model for conti-
965 nental deformation. *Geophys. J. R. Astr. Soc.*, 73:523–532.
- 966 Fagereng, Å. and Biggs, J. (2019). New perspectives on ‘geological strain rates’ calculated
967 from both naturally deformed and actively deforming rocks. *J. Struct. Geol.*, 125(January
968 2018):100–110.
- 969 Fielding, E. J. and McKenzie, D. (2012). Lithospheric flexure in the Sichuan Basin and
970 Longmen Shan at the eastern edge of Tibet. *Geophys. Res. Lett.*, 39:L09311.
- 971 Flesch, L., Bendick, R., and Bischoff, S. (2018). Limitations on Inferring 3D Architecture
972 and Dynamics From Surface Velocities in the India-Eurasia Collision Zone. *Geophys. Res.*
973 *Lett.*, 45:1379–1386.

- 974 Flesch, L. M., Haines, J. A., and Holt, W. E. (2001). Dynamics of the India-Eurasia Short-
975 ening. *J. Geophys. Res.*, 106(B8):16,435–16,460.
- 976 Gourbet, L., Hervé, P., Paquette, J.-L., Sorrel, P., Maheo, G., Wang, G., Yadong, X.,
977 Cao, K., Antoine, P.-O., Eymard, I., Liu, W., Lu, H., Replumaz, A., Chevalier, M.-L.,
978 Kexin, Z., Jing, W., and Shen, T. (2017). Reappraisal of the Jianchuan Cenozoic basin
979 stratigraphy and its implications on the SE Tibetan plateau evolution. *Tectonophysics*,
980 700-701:162–179.
- 981 Gratton, J., Minotti, F., and Mahajan, S. M. (1999). Theory of creeping gravity currents of
982 a non-Newtonian liquid. *Phys. Rev. E - Stat. Physics, Plasmas, Fluids, Relat. Interdiscip.*
983 *Top.*, 60(6):6960–6967.
- 984 Han, L., Cheng, J., An, Y., Fang, L., Jiang, C., Chen, B., Wu, Z., Liu, J., Xu, X., Liu, R.,
985 Yao, Z., Wang, C., and Wang, Y. (2018). Preliminary Report on the 8 August 2017 Ms
986 7.0 Jiuzhaigou, Sichuan, China, Earthquake. *Seismol. Res. Lett.*, 89(2A):557–569.
- 987 Han, L., Zeng, X., Jiang, C., Ni, S., Zhang, H., and Long, F. (2014). Focal Mechanisms of
988 the 2013 Mw 6.6 Lushan, China Earthquake and High-Resolution Aftershock Relocations.
989 *Seismol. Res. Lett.*, 85(1):8–14.
- 990 Hirth, G. and Kohlstedt, D. (2003). Rheology of the upper mantle and the mantle wedge:
991 A view from the experimentalists. *Geophys. Monogr. Ser.*, 138:83–105.
- 992 Hoke, G. D. (2018). Geochronology transforms our view of how Tibet’s southeast margin
993 evolved. *Geology*, 46(1):95–96.
- 994 Hoke, G. D., Liu-Zeng, J., Hren, M. T., Wissink, G. K., and Garzzone, C. N. (2014). Stable
995 isotopes reveal high southeast Tibetan Plateau margin since the Paleogene. *Earth Planet.*
996 *Sci. Lett.*, 394:270–278.

- 997 Holmes, A. (1965). *The Principles of Physical Geology*. Nelson, Edinburgh.
- 998 Houseman, G. and England, P. (1986). Finite strain calculations of continental deformation.
999 1. Method and general results for convergence zones. *J. Geophys. Res.*, 91(B3):3651–3663.
- 1000 Hren, M. T., Bookhagen, B., Blisniuk, P. M., Booth, A. L., and Chamberlain, C. P. (2009).
1001 $\delta^{18}\text{O}$ and δD of streamwaters across the Himalaya and Tibetan Plateau: Implications for
1002 moisture sources and paleoelevation reconstructions. *Earth Planet. Sci. Lett.*, 288:20–32.
- 1003 Huang, M. H., Bürgmann, R., and Freed, A. M. (2014). Probing the lithospheric rheology
1004 across the eastern margin of the Tibetan Plateau. *Earth Planet. Sci. Lett.*, 396:88–96.
- 1005 Hubbard, J. and Shaw, J. H. (2009). Uplift of the Longmen Shan and Tibetan plateau, and
1006 the 2008 Wenchuan ($M = 7.9$) earthquake. *Nature*, 458(7235):194–197.
- 1007 Hubbard, J., Shaw, J. H., and Klinger, Y. (2010). Structural setting of the 2008 Mw7.9
1008 Wenchuan, China, earthquake. *Bull. Seismol. Soc. Am.*, 100(5B):2713–2735.
- 1009 Huppert, H. E. (1982). The propagation of two-dimensional and axisymmetric viscous gravity
1010 currents over a rigid horizontal surface. *J. Fluid Mech.*, 121:43–58.
- 1011 International Seismological Centre (2016). EHB Bulletin.
- 1012 Jackson, J., McKenzie, D., Priestley, K., and Emmerson, B. (2008). New views on the
1013 structure and rheology of the lithosphere. *J. Geol. Soc. London.*, 165:453–465.
- 1014 Jordan, T. A. and Watts, A. B. (2005). Gravity anomalies, flexure and the elastic thickness
1015 structure of the India-Eurasia collisional system. *Earth Planet. Sci. Lett.*, 236(3-4):732–
1016 750.
- 1017 Kanamori, H. and Anderson, D. (1975). Theoretical basis of some empirical relations in
1018 seismology. *B. Seism. Soc. Am.*, 65(5):1073–1095.

- 1019 Kirby, E., Reiners, P. W., Krol, M. A., Whipple, K. X., Hodges, K. V., Farley, K. A., Tang,
1020 W., and Chen, Z. (2002). Late Cenozoic evolution of the eastern margin of the Tibetan
1021 Plateau: Inferences from $^{40}\text{Ar}/^{39}\text{Ar}$ and (U-Th)/He thermochronology. *Tectonics*,
1022 21(1):1001–1019.
- 1023 Koons, P. O. (1989). The topographic evolution of collisional mountain belts: a numerical
1024 look at the Southern Alps, New Zealand. *Am. J. Sci.*, 289(9):1041–1069.
- 1025 Lamb, S. (2000). Active deformation in the Bolivian Andes, South America. *J. Geophys.*
1026 *Res. Solid Earth*, 105(B11):25627–25653.
- 1027 Lebedev, S. and Nolet, G. (2003). Upper mantle beneath Southeast Asia from S velocity
1028 tomography. *J. Geophys. Res. Solid Earth*, 108(B1).
- 1029 Lechmann, S. M., May, D. A., Kaus, B. J., and Schmalholz, S. M. (2011). Comparing
1030 thin-sheet models with 3-D multilayer models for continental collision. *Geophys. J. Int.*,
1031 187(1):10–33.
- 1032 Lechmann, S. M., Schmalholz, S. M., Hetényi, G., May, D. A., and Kaus, B. J. P. (2014).
1033 Quantifying the impact of mechanical layering and underthrusting on the dynamics of the
1034 modern India-Asia collisional system with 3-D numerical models. *J. Geophys. Res. Solid*
1035 *Earth*, 119(1):616–644.
- 1036 Li, C. and Van Der Hilst, R. D. (2010). Structure of the upper mantle and transition
1037 zone beneath Southeast Asia from traveltimes tomography. *J. Geophys. Res. Solid Earth*,
1038 115(7):1–19.
- 1039 Li, S., Currie, B. S., Rowley, D. B., and Ingalls, M. (2015). Cenozoic paleoaltimetry of the
1040 SE margin of the Tibetan Plateau: Constraints on the tectonic evolution of the region.
1041 *Earth Planet. Sci. Lett.*, 432:415–424.

- 1042 Li, S., Su, T., Spicer, R. A., Xu, C., Sherlock, S., Halton, A., Hoke, G., Tian, Y., Zhang, S.,
1043 Zhou, Z., Deng, C., and Zhu, R. (2020). Oligocene deformation of the Chuandian terrane
1044 in the SE margin of the Tibetan Plateau related to the extrusion of Indochina. *Tectonics*,
1045 pages 0–3.
- 1046 Li, Z., Elliott, J. R., Feng, W., Jackson, J. A., Parsons, B. E., and Walters, R. J. (2011).
1047 The 2010 Mw 6.8 Yushu (Qinghai, China) earthquake: Constraints provided by InSAR
1048 and body wave seismology. *J. Geophys. Res. Solid Earth*, 116:B10302.
- 1049 Licht, A., Botsyun, S., Littell, V., Sepulchre, P., Donnadieu, Y., Risi, C., Rugenstein, J.
1050 K. C., Page, M., Huntington, K. W., and Nivet, G. D. (2019). Is Tibetan Plateau uplift
1051 more recent than we thought? In *AGU Fall Meet. Abstr.*
- 1052 Licht, A., van Cappelle, M., Abels, H. A., Ladant, J.-B., Trabucho-Alexandre, J., France-
1053 Lanord, C., Donnadieu, Y., Vandenberghe, J., Rigaudier, T., Lécuyer, C., Terry Jr, D.,
1054 Adriaens, R., Boura, A., Guo, Z., Soe, A. N., Quade, J., Dupont-Nivet, G., and Jaeger,
1055 J.-J. (2014). Asian monsoons in a late Eocene greenhouse world. *Nature*, 513(7519):501–
1056 506.
- 1057 Liu, C. Z., Wu, F. Y., Sun, J., Chu, Z. Y., and Yu, X. H. (2013). Petrology, geochemistry
1058 and ReOs isotopes of peridotite xenoliths from Maguan, Yunnan Province: Implications
1059 for the Cenozoic mantle replacement in southwestern China. *Lithos*, 168-169:1–14.
- 1060 Liu, Q. Y., van der Hilst, R. D., Li, Y., Yao, H. J., Chen, J. H., Guo, B., Qi, S. H., Wang,
1061 J., Huang, H., and Li, S. C. (2014). Eastward expansion of the Tibetan Plateau by crustal
1062 flow and strain partitioning across faults. *Nat. Geosci.*, 7:361–365.
- 1063 Liu-Zeng, J., Tapponnier, P., Gaudemer, Y., and Ding, L. (2008). Quantifying landscape
1064 differences across the Tibetan plateau: Implications for topographic relief evolution. *J.*
1065 *Geophys. Res. Earth Surf.*, 113:F04018.

- 1066 Liu-Zeng, J., Zhang, J., McPhillips, D., Reiners, P., Wang, W., Pik, R., Zeng, L., Hoke, G.,
1067 Xie, K., Xiao, P., Zheng, D., and Ge, Y. (2018). Multiple episodes of fast exhumation since
1068 Cretaceous in southeast Tibet, revealed by low-temperature thermochronology. *Earth*
1069 *Planet. Sci. Lett.*, 490:62–76.
- 1070 Maurin, T., Masson, F., Rangin, C., Min, U. T., and Collard, P. (2010). First global
1071 positioning system results in northern Myanmar: Constant and localized slip rate along
1072 the Sagaing fault. *Geology*, 38(7):591–594.
- 1073 McGroder, M. F., Lease, R. O., and Pearson, D. M. (2014). Along-strike variation in struc-
1074 tural styles and hydrocarbon occurrences, Subandean fold-and-thrust belt and inner fore-
1075 land, Colombia to Argentina. In *Geol. Soc. Am. Mem.*, volume 212, pages 79–113.
- 1076 McKenzie, D., Jackson, J., and Priestley, K. (2005). Thermal structure of oceanic and
1077 continental lithosphere. *Earth Planet. Sci. Lett.*, 233:337–349.
- 1078 McKenzie, D., McKenzie, J., and Fairhead, D. (2019). The Mechanical Structure of Tibet.
1079 *Geophys. J. Int.*, pages 950–969.
- 1080 McKenzie, D., Nimmo, F., Jackson, J. A., Gans, P. B., and Miller, E. L. (2000). Char-
1081 acteristics and consequences of flow in the lower crust. *J. Geophys. Res. Solid Earth*,
1082 105(B5):11029–11046.
- 1083 McKenzie, D. and Priestley, K. (2008). The influence of lithospheric thickness variations on
1084 continental evolution. *Lithos*, 102:1–11.
- 1085 Medvedev, S. E. and Podladchikov, Y. Y. (1999a). New extended thin-sheet approximation
1086 for geodynamic applications—I. Model formation. *Geophys. J. Int.*, 136(3):586–608.
- 1087 Medvedev, S. E. and Podladchikov, Y. Y. (1999b). New extended thin-sheet approximation

- 1088 for geodynamic applications-II. Two-dimensional examples. *Geophys. J. Int.*, 136(3):586–
1089 608.
- 1090 Merle, O. and Guillier, B. (1989). The building of the Central Swiss Alps: an experimental
1091 approach. *Tectonophysics*, 165(1-4):41–56.
- 1092 Miller, K. G., Fairbanks, R. G., and Mountain, G. S. (1987). Tertiary Oxygen Isotope
1093 Synthesis, Sea Level History, and Continental Margin Erosion. *Paleoceanography*, 2(1):1–
1094 19.
- 1095 Molnar, P. and Lyon-Caen, H. (1988). Some simple physical aspects of the support, structure,
1096 and evolution of mountain belts. In *GSA Spec. Pap.*, volume 218, pages 179–208.
- 1097 Molnar, P. and Tapponnier, P. (1978). Active Tectonics of Tibet. *J. Geophys. Res.*, 83(B11).
- 1098 Nissen, E., Tatar, M., Jackson, J., and Allen, M. (2011). New views on earthquake faulting
1099 in the Zagros fold-and-thrust belt of Iran. *Geophys. J. Int.*, 186:928–944.
- 1100 Pattyn, F. (2003). A new three-dimensional higher-order thermomechanical ice sheet model:
1101 Basic sensitivity, ice stream development, and ice flow across subglacial lakes. *J. Geophys.*
1102 *Res.*, 108(B8):1–15.
- 1103 Pusok, A. E. and Kaus, B. J. P. (2015). Development of topography in 3-D continental-
1104 collision models. *Geochemistry, Geophysics, Geosystems*, 16(5):1378–1400.
- 1105 Ramberg, H. (1981). The role of gravity in orogenic belts. *Geol. Soc. Spec. Publ.*, 9:125–140.
- 1106 Reynolds, K., Copley, A., and Hussain, E. (2015). Evolution and dynamics of a fold-thrust
1107 belt: The Sulaiman Range of Pakistan. *Geophys. J. Int.*, 201:683–710.
- 1108 Richardson, N. J., Densmore, A. L., Seward, D., Fowler, A., Wipf, M., Ellis, M. A., Yong,
1109 L., and Zhang, Y. (2008). Extraordinary denudation in the Sichuan Basin: Insights from

- 1110 low-temperature thermochronology adjacent to the eastern margin of the Tibetan Plateau.
1111 *J. Geophys. Res. Solid Earth*, 113:B04409.
- 1112 Rowley, D. B. and Currie, B. S. (2006). Palaeo-altimetry of the late Eocene to Miocene
1113 Lunpola basin, central Tibet. *Nature*, 439:677–681.
- 1114 Rowley, D. B., Pierrehumbert, R. T., and Currie, B. S. (2001). A new approach to stable
1115 isotope-based paleoaltimetry: Implications for paleoaltimetry and paleohypsometry of the
1116 High Himalaya since the late Miocene. *Earth Planet. Sci. Lett.*, 188:253–268.
- 1117 Royden, L. H., Burchfiel, B. C., King, R. W., Wang, E., Chen, Z., Shen, F., and Liu, Y.
1118 (1997). Surface Deformation and Lower Crustal Flow in Eastern Tibet. *Science (80-.)*,
1119 276(5313):788–790.
- 1120 Rybacki, E., Gottschalk, M., Wirth, R., and Dresen, G. (2006). Influence of water fugacity
1121 and activation volume on the flow properties of fine-grained anorthite aggregates. *J.*
1122 *Geophys. Res. Solid Earth*, 111(3).
- 1123 Saad, Y. and Schultz, M. H. (1986). GMRES: A Generalized Minimal Residual Algorithm
1124 for Solving Nonsymmetric Linear Systems. *SIAM J. Sci. Stat. Comput.*, 7(3):856–869.
- 1125 Savin, S. M. (1977). The History of the Earth’s Surface Temperature During the Past 100
1126 Million Years. *Annu. Rev. Earth Planet. Sci.*, 5(1):319–355.
- 1127 Schmalholz, S. M., Medvedev, S., Lechmann, S. M., and Podladchikov, Y. (2014). Relation-
1128 ship between tectonic overpressure, deviatoric stress, driving force, isostasy and gravita-
1129 tional potential energy. *Geophys. J. Int.*, 197(2):680–696.
- 1130 Shen, Z. K., Lü, J., Wang, M., and Bürgmann, R. (2005). Contemporary crustal deformation
1131 around the southeast borderland of the Tibetan Plateau. *J. Geophys. Res. Solid Earth*,
1132 110:B11409.

- 1133 Sonder, L. J. and England, P. (1986). Vertical averages of rheology of the continental
1134 lithosphere: relation to thin sheet parameters. *Earth Planet. Sci. Lett.*, 77:81–90.
- 1135 Steckler, M. S., Mondal, D. R., Akhter, S. H., Seeber, L., Feng, L., Gale, J., Hill, E. M., and
1136 Howe, M. (2016). Locked and loading megathrust linked to active subduction beneath the
1137 Indo-Burman Ranges. *Nat. Geosci.*, 9:615–618.
- 1138 Stocker, R. L. and Ashby, M. F. (1973). On the rheology of the upper mantle. *Rev. Geophys.*,
1139 11(2):391–426.
- 1140 Stork, A. L., Selby, N. D., Heyburn, R., and Searle, M. P. (2008). Accurate relative earth-
1141 quake hypocenters reveal structure of the Burma subduction zone. *Bull. Seismol. Soc.*
1142 *Am.*, 98(6):2815–2827.
- 1143 Tang, M., Liu-Zeng, J., Hoke, G. D., Xu, Q., Wang, W., Li, Z., Zhang, J., and Wang, W.
1144 (2017). Paleoelevation reconstruction of the Paleocene-Eocene Gonjo basin, SE-central
1145 Tibet. *Tectonophysics*, 712-713:170–181.
- 1146 Vilotte, J. P., Daignieres, M., Madariaga, R., and Zienkiewicz, O. C. (1984). The role of a
1147 heterogeneous inclusion during continental collision. *Phys. Earth Planet. Inter.*, 36:236–
1148 259.
- 1149 Wang, E. and Burchfiel, B. C. (1997). Interpretation of Cenozoic Tectonics in the Right-
1150 Lateral Accommodation Zone Between the Ailao Shan Shear Zone and the Eastern Hi-
1151 malayan Syntaxis. *Int. Geol. Rev.*, 39(3):191–219.
- 1152 Wang, E., Kirby, E., Furlong, K. P., Van Soest, M., Xu, G., Shi, X., Kamp, P. J. J., and
1153 Hodges, K. V. (2012). Two-phase growth of high topography in eastern Tibet during the
1154 Cenozoic. *Nat. Geosci.*, 5:640–645.

- 1155 Wang, Y., Sieh, K., Tun, S. T., Lai, K.-Y., and Myint, T. (2014). Active tectonics and
1156 earthquake potential of the Myanmar region. *J. Geophys. Res. Solid Earth*, 119:3767–
1157 3822.
- 1158 Wang, Y., Zhang, B., Schoenbohm, L. M., Zhang, J., Zhou, R., Hou, J., and Ai, S. (2016).
1159 Late Cenozoic tectonic evolution of the Ailao Shan-Red River fault (SE Tibet): Implica-
1160 tions for kinematic change during plateau growth. *Tectonics*, 35:1969–1988.
- 1161 Wessel, P., Smith, W. H. F., Scharroo, R., Luis, J., and Wobbe, F. (2013). Generic Mapping
1162 Tools: Improved version released. *EOS Trans. AGU*, 94(45):409–410.
- 1163 Wimpenny, S., Copley, A., Benavente Escobar, C. L., and Aguirre, E. (2018). Extension
1164 and Dynamics of the Andes inferred from the 2016 Parina (Huarichancara) Earthquake.
1165 *J. Geophys. Res. Solid Earth*, pages 1–31.
- 1166 Wittlinger, G., Vergne, J., Tapponnier, P., Farra, V., Poupinet, G., Jiang, M., Su, H.,
1167 Herquel, G., and Paul, A. (2004). Teleseismic imaging of subducting lithosphere and
1168 Moho offsets beneath western Tibet. *Earth Planet. Sci. Lett.*, 221(1-4):117–130.
- 1169 Wu, J., Zhang, K., Xu, Y., Wang, G., Garzzone, C. N., Eiler, J., Leloup, P. H., Sorrel, P.,
1170 and Mahéo, G. (2018). Paleoelevations in the Jianchuan Basin of the southeastern Tibetan
1171 Plateau based on stable isotope and pollen grain analyses. *Palaeogeogr. Palaeoclimatol.*
1172 *Palaeoecol.*, 510(March):93–108.
- 1173 Xiong, Z., Ding, L., Spicer, R. A., Farnsworth, A., Wang, X., Valdes, P. J., Su, T., Zhang,
1174 Q., Zhang, L., Cai, F., Wang, H., Li, Z., Song, P., Guo, X., and Yue, Y. (2020). The early
1175 Eocene rise of the Gonjo Basin, SE Tibet: From low desert to high forest. *Earth Planet.*
1176 *Sci. Lett.*, 543:116312.
- 1177 Xu, Q., Liu, X., and Ding, L. (2016). Miocene high-elevation landscape of the eastern
1178 Tibetan Plateau. *Geochemistry, Geophys. Geosystems*, 17(10):4254–4267.

- 1179 Xu, X., Ding, Z., Shi, D., and Li, X. (2013). Receiver function analysis of crustal structure
1180 beneath the eastern Tibetan plateau. *J. Asian Earth Sci.*, 73:121–127.
- 1181 Yang, R., Willett, S. D., and Goren, L. (2015). In situ low-relief landscape formation as a
1182 result of river network disruption. *Nature*, 520:526–529.
- 1183 Yu, H. M., Lin, C. Y., Shi, L. B., Xu, J. D., and Chen, X. D. (2010). Characteristics and
1184 origin of mafic and ultramafic xenoliths in trachyandesite lavas from Heikongshan volcano,
1185 Tengchong, Yunnan Province, China. *Sci. China Earth Sci.*, 53(9):1295–1306.
- 1186 Zachos, J., Pagani, H., Sloan, L., Thomas, E., and Billups, K. (2001). Trends, rhythms, and
1187 aberrations in global climate 65 Ma to present. *Science (80-.)*, 292(5517):686–693.
- 1188 Zhang, P.-Z., Wen, X.-Z., Shen, Z.-K., and Chen, J.-H. (2010). Oblique, High-Angle, Listric-
1189 Reverse Faulting and Associated Development of Strain: The Wenchuan Earthquake of
1190 May 12, 2008, Sichuan, China. *Annu. Rev. Earth Planet. Sci.*, 38(1):353–382.
- 1191 Zheng, G., Wang, H., Wright, T. J., Lou, Y., Zhang, R., Zhang, W., Shi, C., Huang, J., and
1192 Wei, N. (2017). Crustal Deformation in the India-Eurasia Collision Zone From 25 Years
1193 of GPS Measurements. *J. Geophys. Res. Solid Earth*, 122(11):9290–9312.

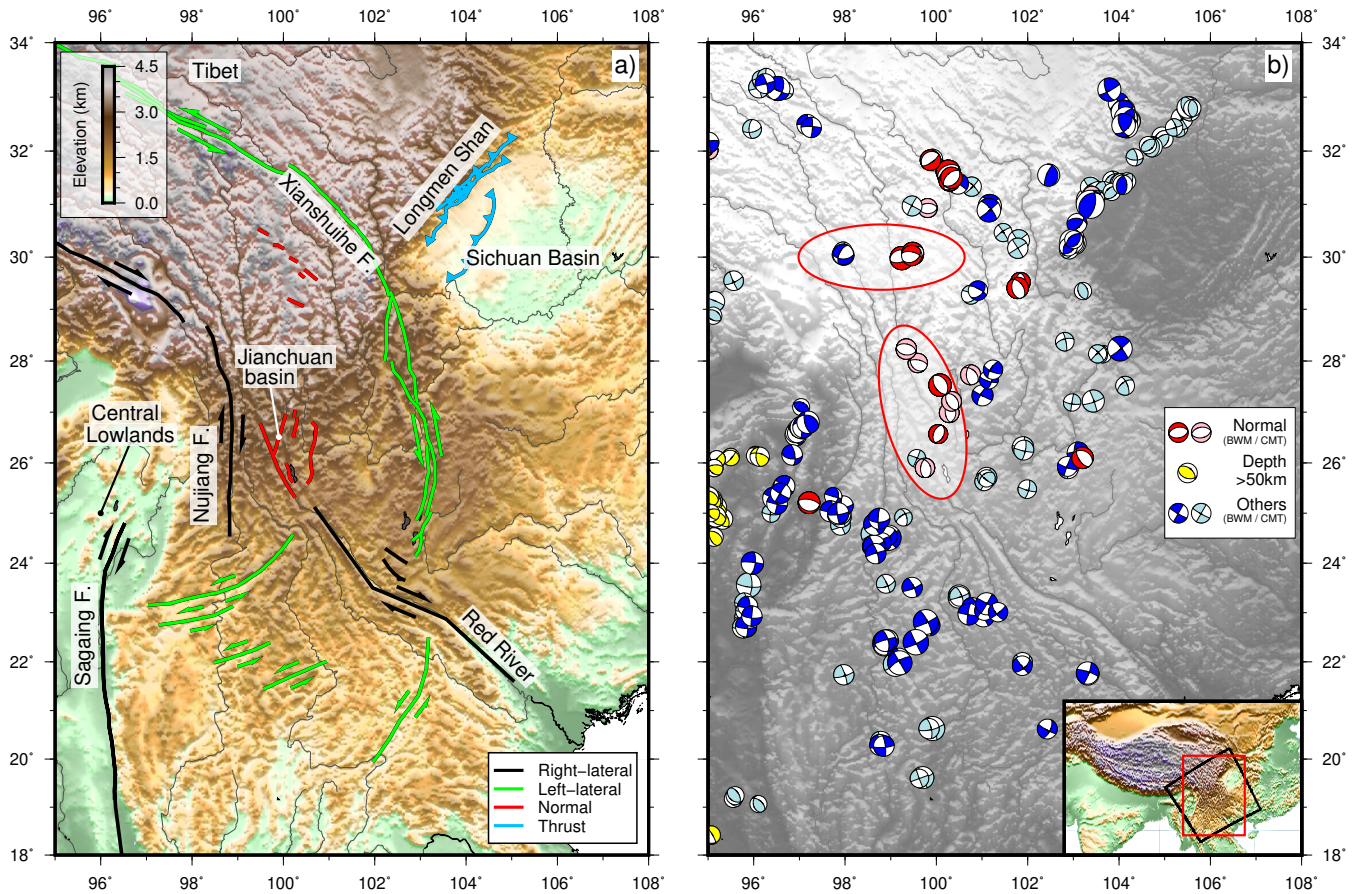


Figure 1: a) Major active faults in south-east Tibet, from Copley (2008); Hubbard and Shaw (2009) and references therein. Black and green lines are right- and left-lateral strike-slip faults respectively. Note the opposite sense of shear adjacent to the Central Lowlands of Myanmar and Sichuan Basin. Red lines show normal faults. Blue lines show thrust faults with teeth on the hanging-wall side. b) Focal mechanisms of earthquakes in south-east Tibet. Focal mechanisms determined from body-waveform modelling from Copley (2008) (and references therein), Zhang et al. (2010), Li et al. (2011), Han et al. (2014), Bai et al. (2017), Han et al. (2018) are shown in red if they have a rake of $-90 \pm 35^\circ$ (normal faulting), and dark blue otherwise. Yellow focal mechanisms are >50 km deep and are associated with subduction beneath the Indo-Burman ranges, most other earthquakes have depths less than ~ 20 km. Focal mechanisms in pink (normal faulting, with rakes of $-90 \pm 35^\circ$) and pale blue are those from the CMT catalogue up to May 2016 with $>70\%$ double couple and >10 depth phases in the EHB catalogue if the earthquake occurred before 2009. Two regions of normal faulting discussed in the text are circled in red. Red box in inset shows the figure's location, black box shows location of Figure 3.

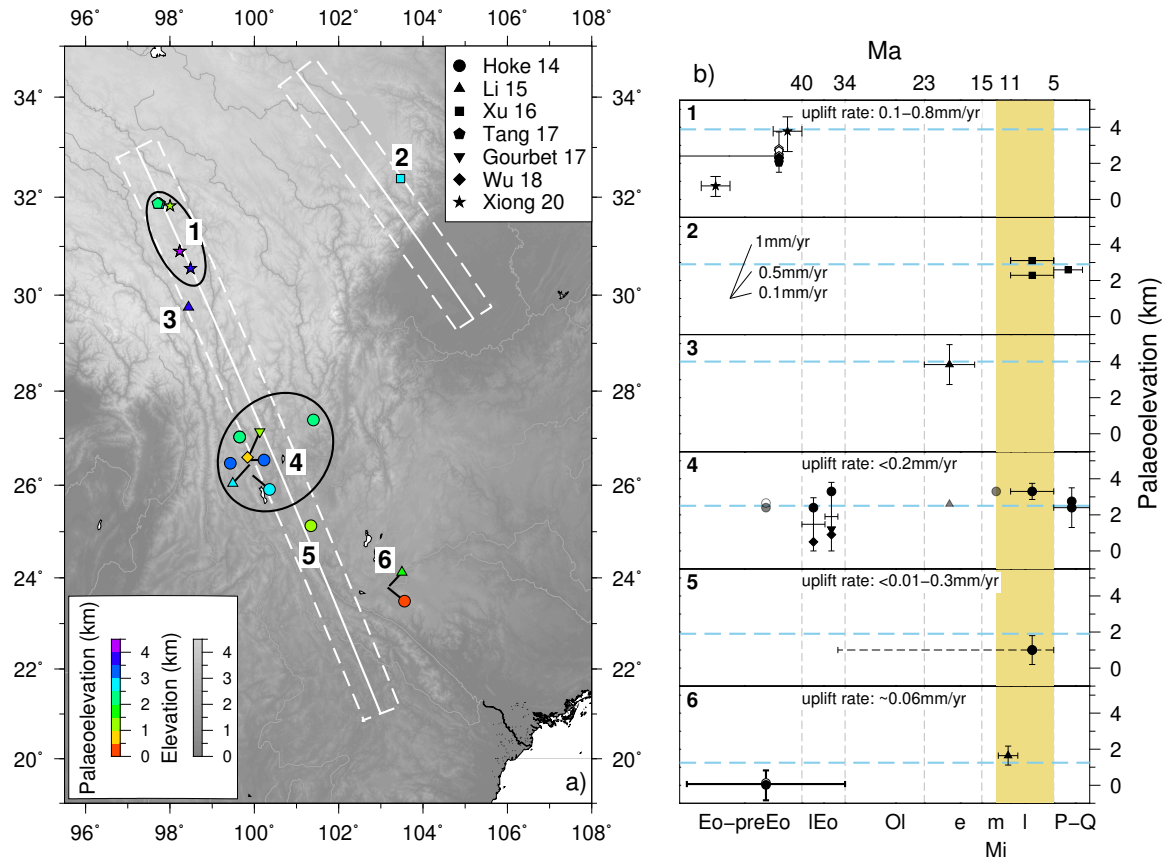


Figure 2: Results of stable-isotope palaeoaltimetry studies in south-east Tibet. a) Sample localities from Hoke et al. (2014); Li et al. (2015); Xu et al. (2016); Tang et al. (2017); Gourbet et al. (2017) and Wu et al. (2018) are coloured by palaeoelevation. 6 regions are labelled, which correspond to panels in b, ellipses indicate the extents of regions 1 (Gonjo Basin) & 4 (Jianchuan and surrounding basins). White lines and boxes show the regions plotted as topographic profiles in Figure 6g and h. b) Sample ages and palaeoelevations in each region. Epoch labels are – Eo-preEo: Eocene-pre Eocene >40 Ma, IEo: late Eocene: 40–34 Ma, Ol: Oligocene 34–23 Ma, eMi: early Miocene 23–15 Ma, mMi: middle Miocene 15–11 Ma, lMi: late Miocene 7–5 Ma, P-Q: Pliocene–Quaternary 5–0 Ma. Symbol shapes are as in a). Yellow bar shows the timing of increased exhumation and erosion rates suggested by Clark et al. (2005b) to indicate rapid uplift. Dashed blue lines indicate mean present-day sample-site elevation for each region. Where multiple samples from the same author are reported in the same epoch in the same region only a single error bar (representing the highest and lowest palaeoelevation estimates) is plotted. Palaeoelevation estimates using a modern temperature-elevation relationship are shown as filled symbols, those using a higher Eocene temperature estimate are unfilled. Gray points in region 4 are the authors’ original palaeoelevation/age inferences. Black points in region 4 show the revised palaeoelevations/ages from Gourbet et al. (2017) and Wu et al. (2018), which we use to determine uplift rates. The age error bar in region 5 indicates the reassessment of Li et al. (2020) – those authors did not recalculate the palaeoelevation of the sample based on the revised dating.

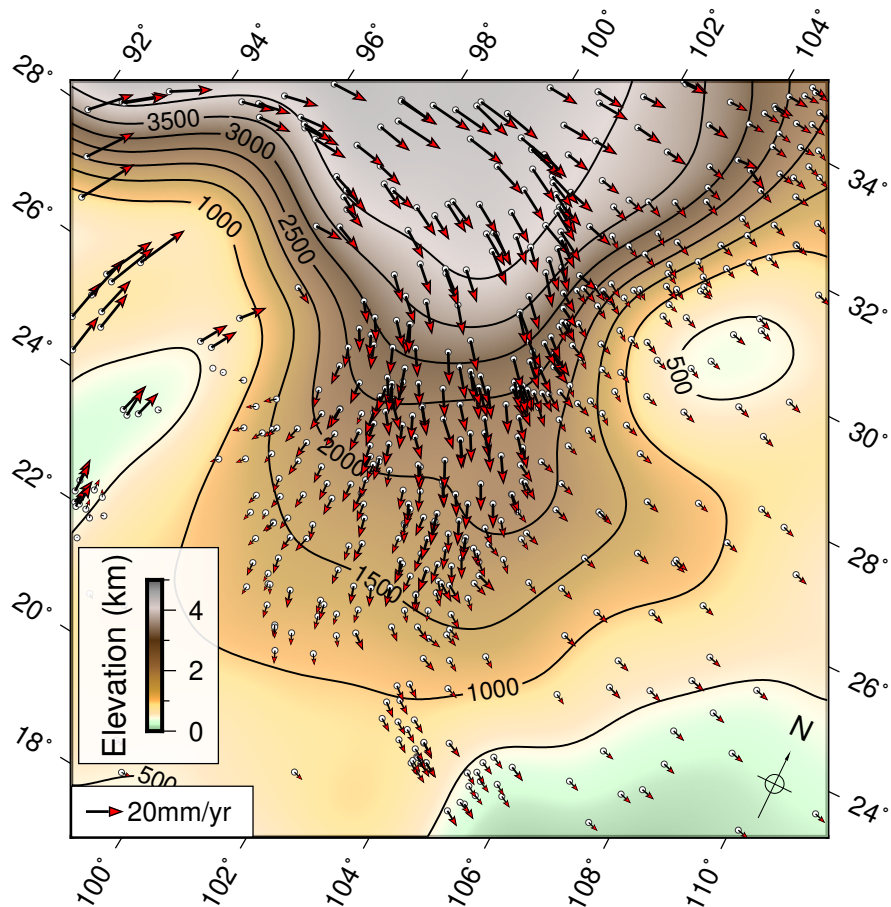


Figure 3: Topography of south-east Tibet after applying a low-pass 500 km-diameter Gaussian filter in an oblique Mercator projection (equator azimuth 60° , centred on 101.5° E, 26.5° N, location shown as black box in the inset of Figure 1b) for comparison to our model set-up (Figure 4) and results (Figures 5 and 8, Section 4). GPS velocities from Zheng et al. (2017) are shown in a Eurasia-fixed reference frame.

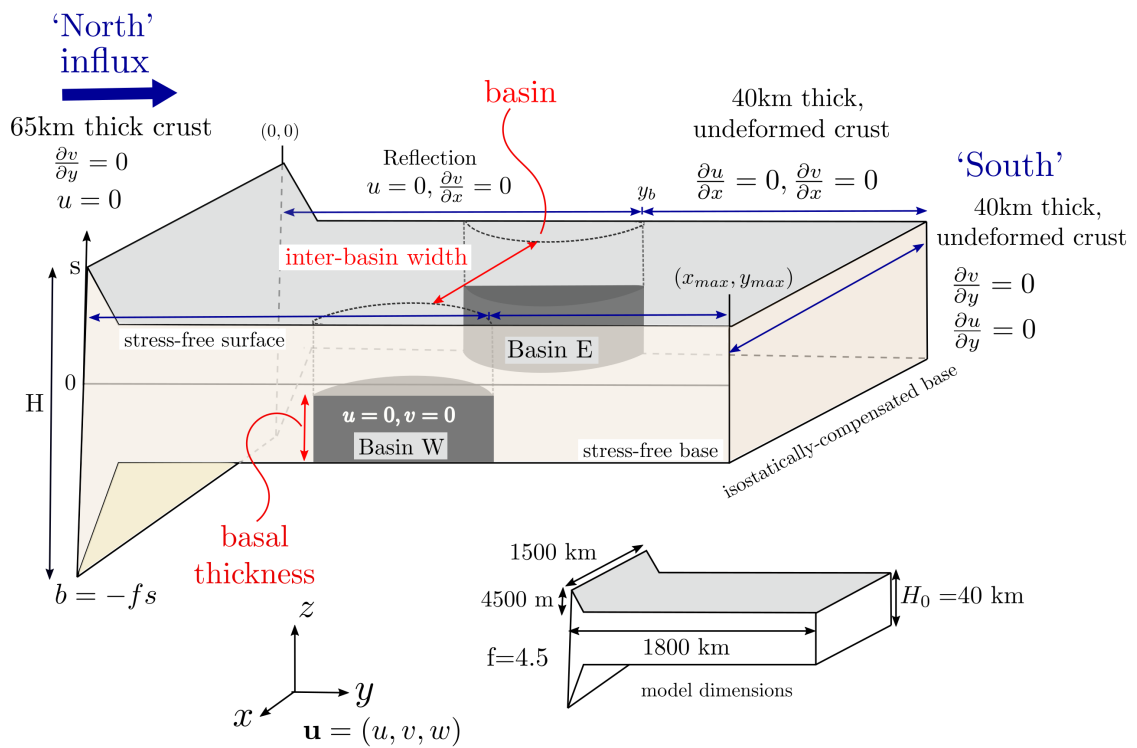


Figure 4: Model geometry, showing the initial topography and symmetric rigid regions. Boundary conditions on $x = x_{max}$ are the same as those on $x = 0$. Inset shows dimensions of model domain. The isostatic root is not shown to scale.

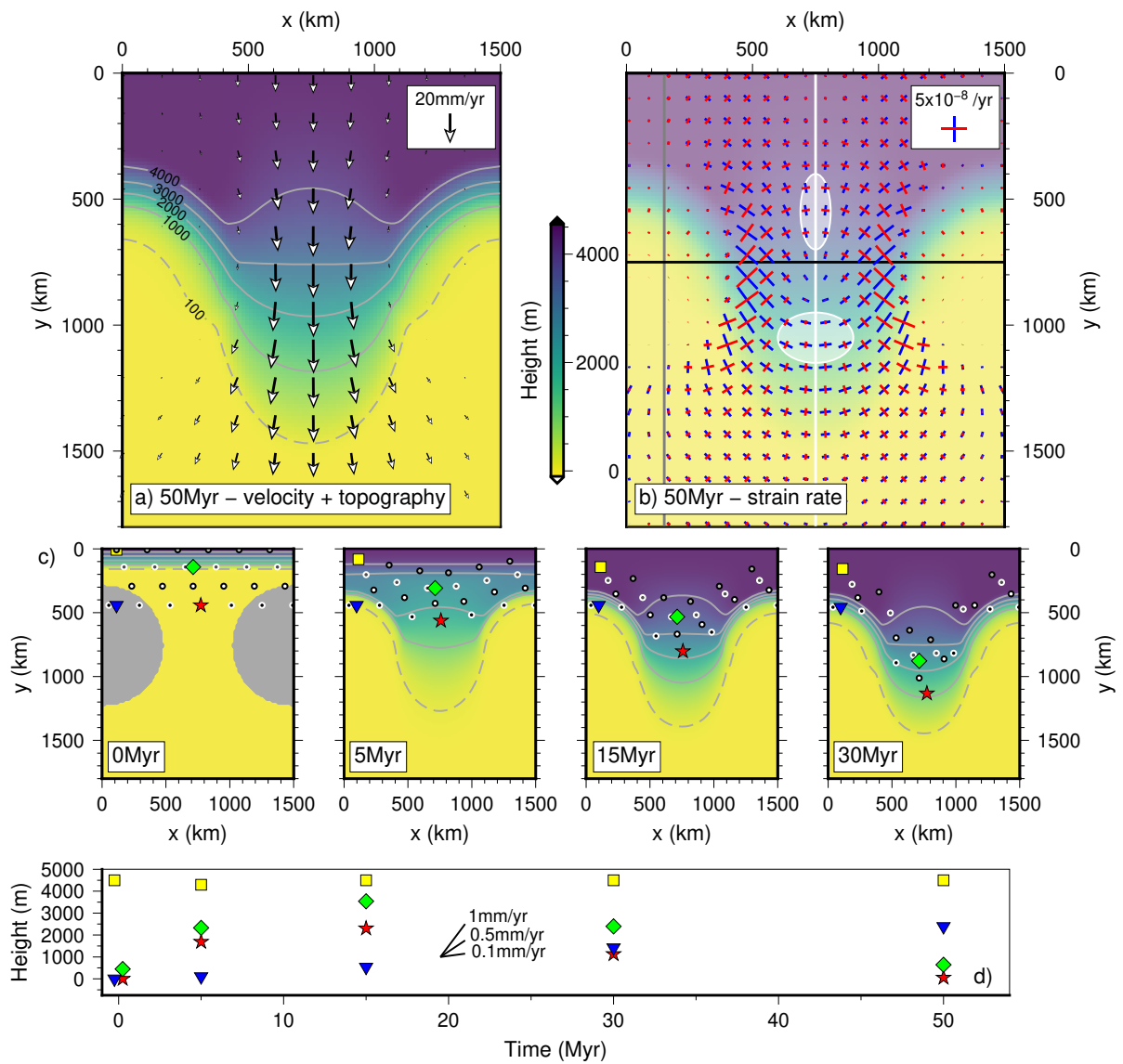


Figure 5: see overleaf

Figure 5: Modelling results for a symmetric model (both basins have the same size and location in y) with 450 km-radius basins (grey semicircles at 0 Myr in c) with a 15 km-thick rigid base. The influx boundary (left-hand side in Figure 4) is at the top of each panel. a) topography and velocities after 50 Myr for a fluid with a viscosity of 10^{22} Pas. Topography is plotted relative to the surface of 40 km-thick, isostatically-compensated crust and contoured at 100 m (dashed line), 1000 m, 2000 m, 3000 m and 4000 m. b) principal axes of the surface horizontal strain-rate tensor after 50 Myr. Blue bars are extensional, red bars are compressional. Gray, white and black lines show locations of profiles in Figures 6c, d and 7c respectively. White ellipses show the two regions where extensional strain rates are ~ 2 –5 times greater than compressional strain rates, discussed in Section 5. c) Evolution of topography through time. Dots show large-scale lateral transport of particles moving with the surface of the current and can be viewed as analogous to the motion of near-surface carbonates used for palaeoaltimetry (Section 3.2). d) shows the elevation history of the shaped particles in c. Since the particles are advected with the current their elevation can decrease as well as increase.

Figure 6: Effect of changing the basal thickness of the rigid basin (analogous to the thickness of undeforming lower crust) on the propagation of topography. The locations of these profiles are shown in Figure 5b. The lateral extent of the basin which has a rigid basal thickness is indicated by the grey bars in a, c and e. a), c) and e) show profiles through the basin (gray line in Figure 5b) for basal thicknesses of 0 km (rigid base), 15 km and 30 km respectively. b), d) and f) show profiles through the inter-basin (stress-free base) region (white line in Figure 5b) for basal thicknesses of 0 km (rigid base), 15 km and 30 km respectively. The basal thickness has no significant effect on the development of topography in the regions with stress-free base. Elevations are relative to the surface of 40 km-thick, isostatically-compensated crust. Inset in e) shows the full thickness of the current (10x vertical exaggeration) to demonstrate how topography in this figure relates to full model. Grey region is the rigid basin. Dashed lines in c) and d) show the effect of erosion with $\kappa = 4 \text{ mm yr}^{-1}$ in equation (1). c and d are profiles through the same model shown in Figure 5. g) and h) show topographic profiles and standard deviation across the Longmen Shan and between the Sichuan Basin and Central Lowlands of Myanmar respectively (profile locations shown in Figure 2a), demonstrating the similarity of topographic gradients in south-east Tibet to those resulting from our model.

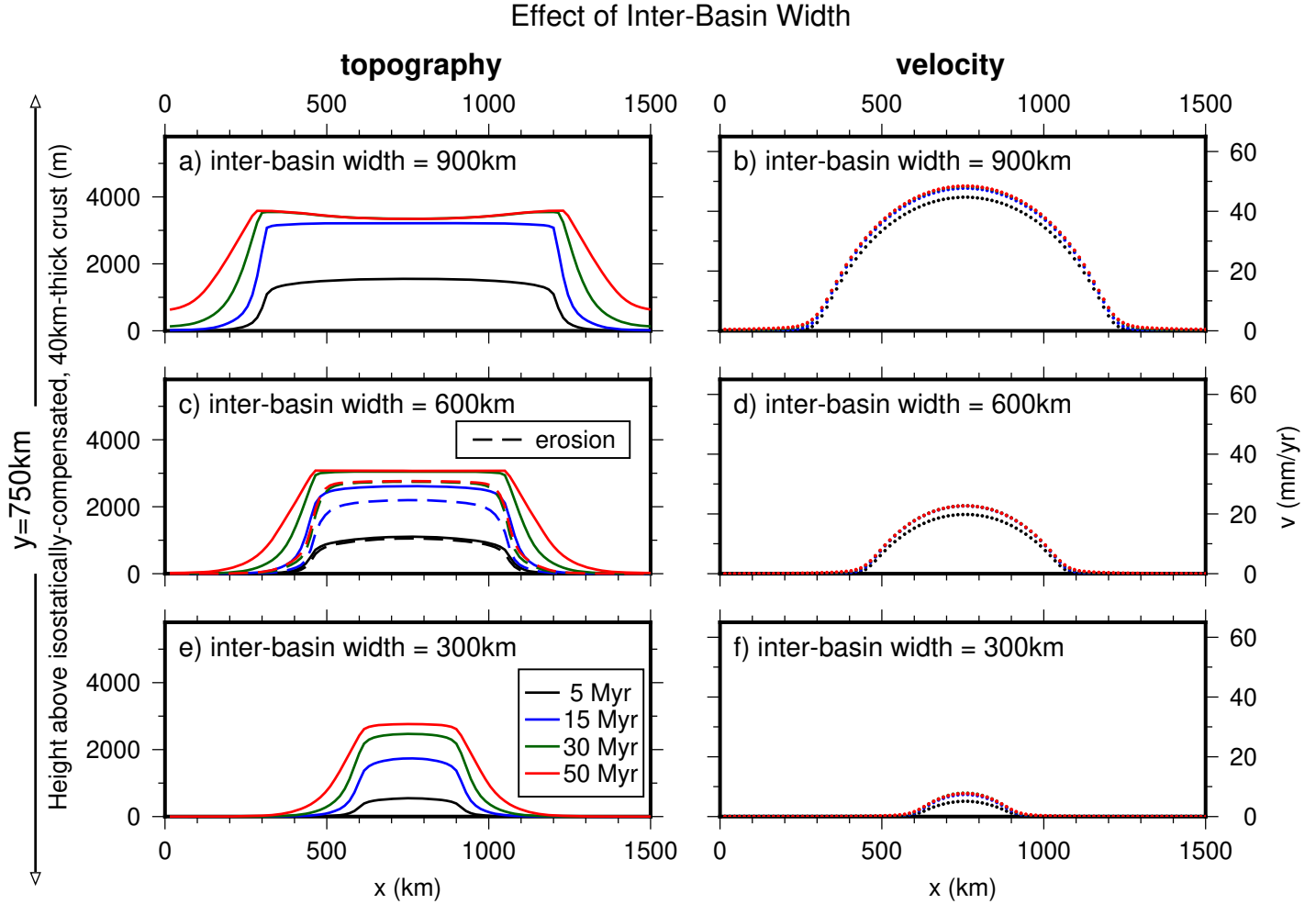


Figure 7: Effect of changing the distance between basins (inter-basin width, Figure 4). In each case profiles are taken at the centre of the semi-circular regions (black line in Figure 5b shows location of c and d), which have a basal thickness of 15 km. Elevations are relative to the surface of 40 km-thick, isostatically-compensated crust. a) and b) 900 km inter-basin width. a) shows the evolution of topography through time. The slight saddle arises because of thinning due to rapid velocities in the centre of the inter-basin region. b) the velocity perpendicular to the profile (v in Figure 4) after 50 Myr. c) and d) as for a and b but for an inter-basin width of 600 km. Note that c) and d) are profiles through the same model as Figure 5 and Figures 6c and d, with basin radius 450 km, inter-basin width 600 km and basal thickness 15 km. Dashed lines show the effects of erosion with $\kappa = 4 \text{ mm yr}^{-1}$ in equation (1). e) and f) as for a and b but for an inter-basin width of 300 km.

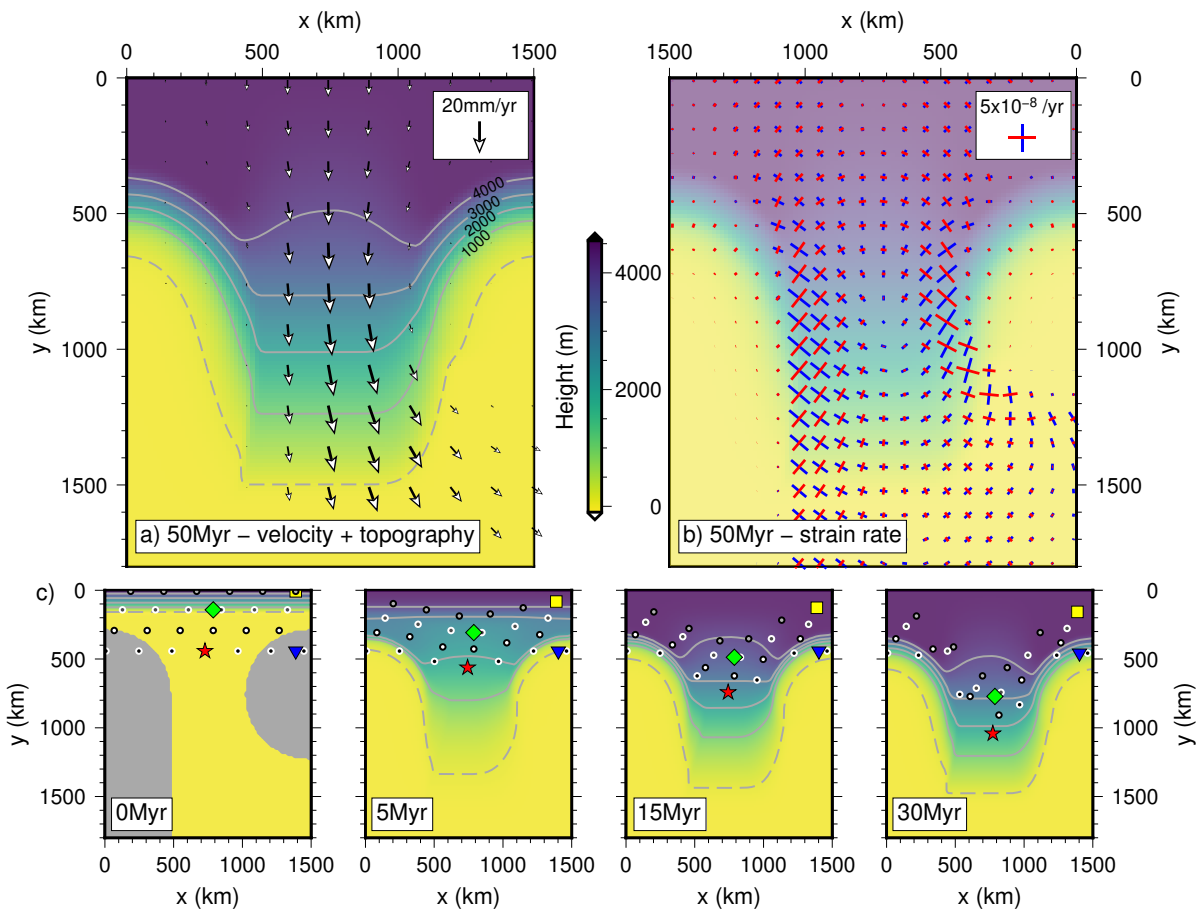


Figure 8: Modelling results for an asymmetric model set-up with 15 km basal thickness in the regions shown in grey in the 0 Myr panel of c. Panels are as for Figure 5. Note the greater ‘southward’ extent of shear adjacent to the extended basin.

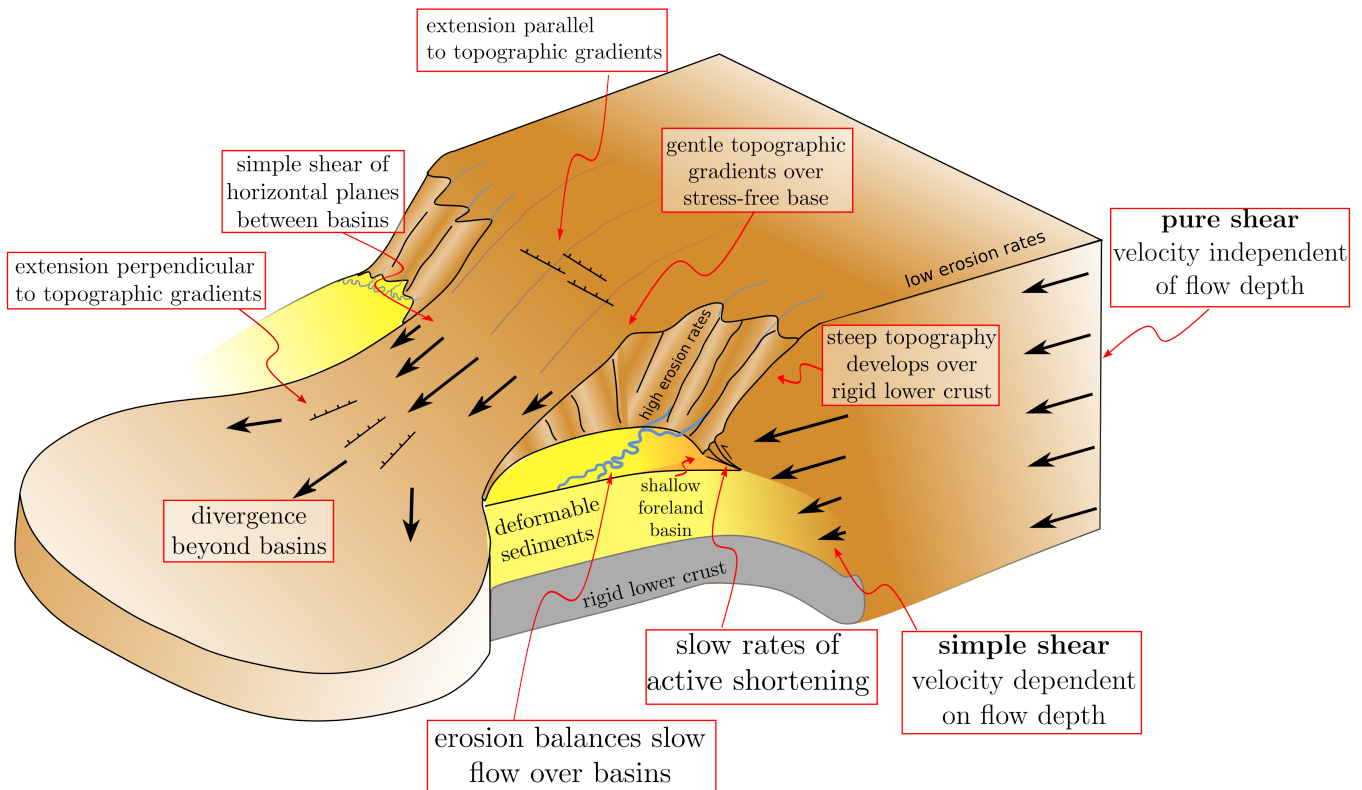


Figure 9: Cartoon showing effects of a rigid region on the development of topography. Steep topographic gradients develop above the region of rigid lower crust because of the dependence of velocity on flow depth. The compressional strain rates associated with growth of this steep topography are much less than the shear strain rates between basins. Regions with a stress-free base (without strong lower crust) deform by pure shear of vertical planes, which results in gentle topographic gradients. Between two rigid regions flow is dominated by simple shear of horizontal planes, similar to flow in a pipe. Beyond the basins the flow can spread out, leading to extension.